# MAGNETOTRANSPORT CHARACTERIZATION OF AL-ALO$_x$-AL JOSEPHSON JUNCTIONS

by

MEHMET KAHRAMAN

Submitted to the Graduate School of Engineering and Natural Sciences

in partial fulfillment of the requirements for the degree of Master of Science.

Sabanci University

Fall 2022

# ABSTRACT

MAGNETOTRANSPORT CHARACTERIZATION OF
AL-ALOx-AL JOSEPHSON JUNCTIONS

Mehmet Kahraman

Physics, M.Sc. Thesis, December 2022

Thesis Supervisor: Prof. İsmet İnönü KAYA

Keywords: Josephson junction. Josephson effect, weak superconductivity, Cooper pair, tunneling, nano-fabrication, nano-device

Superconducting quantum devices have been a widely studied topic for the last few decades due to the potential they possess. The fundamental circuit element of such devices are Josephson junction, which works with the principle of Josephson effect. Josephson junction provides the nonlinearity needed for superconducting quantum devices, and allows us to fabricate such devices using basic circuit elements. Consequently, to be able to further progress in developing superconducting devices, high

quality Josephson junctions are required; to be able to fabricate high quality Josephson junction, a precise and repeatable fabrication process is needed.

In this thesis, fabrication and characterization of Josephson junctions are conducted to investigate the important parameters affecting the quality of junctions, in order to help optimize a fabrication process that is precise and repeatable. The theory and theoretical characteristics of Josephson junction are discussed; the detailed fabrication process, the results, the discussion on the lessons learned and future work is presented.

# ÖZET

AL-$ALO_x$-AL JOSEPHSON EKLEMLERİNİN MANYETO-TAŞINIM KARAKTERİZASYONU

MEHMET KAHRAMAN

Fizik, Yüksek Lisans. Tezi, Aralık 2022

Tez Danışmanı: Prof. Dr. İsmet İnönü KAYA

Anahtar Kelimeler: Josephson eklemi, Josephson etkisi, zayıf süperiletkenlik, Cooper çifti, tünelleme, nano-fabrikasyon, nano-aygıt

Süperiletken kuantum aygıtlar, potansiyelleri sebebiyle son yıllarda yoğun olarak çalışılmaktadır. Bu aygıtların temel devre elemanı ise Josephson etkisi prensibiyle çalışan Josephson eklemidir. Josephson eklemi, süperiletken aygıtlar için gerekli olan non-lineerliği sağlamaktadır ve temel devre elemanları kullanarak bu tüp aygıtları üretmemize imkan vermektedir. Dolayısıyla, süperiletken kuantum aygıtlar geliştirilebilmesi için yüksek kalite Josephson eklemine; yüksek kalite Josephson eklemini sürekli üretebilmek için ise tekrarlanabilir ve kusursuz çalışan üretim methodlarına ihtiyaç duyulmaktadır.

Bu çalışmada, yüksek nitelikli Josephson eklemi yapabilmek amacıyla, üretim parametrelerinin incelenip anlaşılması ve üretim yöntemi geliştirilmesine katkıda bulunmak için Josephson eklemi aygıtları üretilmiş ve karakterizasyonlarını yapılmıştır. Bu tezde, Josephson ekleminin teorisine ve teorik karakteristiklerine ilişkin bilgiler ve kullanılan üretim yöntemleri detaylarıyla anlatılmakta; sonuçlar ve sonuçlara yönelik değerlendirmeler ile öğrenilen dersler ve müteakiben bu konu üzerinde yapılmasının faydalı olacağını değerlendirilen hususlar sunulmaktadır.

## ACKNOWLEDGEMENTS

I would like to thank my advisor, Prof. İsmet İnönü Kaya, for providing me the opportunity of working with advanced instruments under his supervision and for supporting and supervising me during my study. I am grateful to him for the opportunity which has taught me very important skills and knowledge, and help me improve my scientific and critical thinking.

I would like to thank Dr. Cenk Yanık and Süleyman Çelik, who taught me nano-fabrication and helped me whenever I needed. They played a huge part on the development of my experimental skills. I am glad that I had such mentors.

I would like to thank Dr. Vahid Sazgari, Dr. Hadi Khaksaran and, for their support and help during my study. They contributed very strongly in my learning and provided me a great work environment. And they helped me whenever I needed. I am grateful to have worked with them in the same research group.

I would like to thank Ali Osman Çetinkaya, Bülent Köroğlu, Onur Serbest, and Selim Tanrıseven, for their support and help. They always helped me whatever I needed at SUNUM. I am glad to have met them.

I would like to thank my dear friends Tuna Alp, Yasin Öztürk, Ege Aygıt, Neslihan Şişman, Selin Öykü Gündoğdu, Sena Yüce, Öykü Demirel, Sarp Kölgesiz, Mehmet Can Dursun, Reza Firouzmandi, Asena Gülenay Tatar, İpek Deniz Yıldırım, İleyna Üvak, Cem Meriç, Çiğdem Bilici, Ahmet Can Kırlıoğlu and Saifa Amin, for their friendship and support. They have been an important part of my life during my study. They taught me a lot, both about life and about science. Their friendship is invaluable. I am grateful to have met them.

I would like to thank my dear family, my mother, my father, my sisters, and my brothers in law. They always supported me financially and morally and never stop supporting me.

I am thankful to Sabancı University and SUNUM, for the opportunity to study and work at a great environment.

*To my dear family...*

## TABLE OF CONTENT

## LIST OF FIGURES

## LIST OF ABBREVIATIONS

| | |
|---|---|
| Al | : Aluminum |
| $Al_2O_3$ | : Aluminum Oxide (Alumina) |
| $AlO_x$ | : Aluminum Oxide |
| BCS | : Bardeen–Cooper–Schrieffer |
| CAD | : Computer Aided Design |
| DR | : Dilusion Refrigerator |
| EBL | : Electron Beam Lithography |
| IPA | : Isopropyl Alcohol |
| I-V | : Current-Voltage |
| MIBK | : Methyl Isobutyl Ketone |
| PMMA | : Polymethyl Metacrylate |
| PS | : Power Source |
| RCSJ | : Resistively and Capasitively Shunted Junction |
| R-T | : Resistance-Temperature |
| SEM | : Scanning Electron Microscope |
| Si | : Silicon |
| $SiO_2$ | : Silicon Dioxide |
| SIS | : Superconductor-Insulator-Superconductor |
| SMU | : Source Measure Unit |
| SQUID | : Superconducting Quantum Interference Device |
| QUBIT | : Quantum Bit |

# 1. INTRODUCTION

## 1.1 Aim of the Thesis

Josephson Effect is the phenomenon in which superconducting tunneling occurs between two superconductors that are in close proximity which is separated by a very thin barrier such as an insulator or a non-superconducting metal. When superconductors are at superconducting phase, some electrons with equal and opposite spins and momenta pair (Cooper pair) and this results in supercurrent. Then this current tunnel between two superconductors separated with a very thin layer back and forth, generating an AC current even when no voltage is applied [1]. The device in which this phenomenon occurs is called a Josephson junction.

Importance of Josephson junction is since it is the main component of superconducting devices such as quantum bit (qubit) [2]. For example, in order to fabricate an artificial atom using common electronic components, an anharmonic oscillator circuit is needed to be fabricated. Normally LC circuits are used to make an oscillator, but since they are harmonic oscillators it is not applicable for this purpose. By replacing linear inductor component with a non-linear inductor, we can achieve this and as the non-linear inductor a Josephson junction is used. Therefore, there is a huge dependency of quantum device fabrication on Josephson junction. Consequently, fabrication of a reliable Josephson junction is needed.

The aim of this thesis is to fabricate and characterize Josephson junctions; discover what parameters effect the quality of the junction at what extend in order to optimize a fabrication method in the future. We worked on superconductor-insulator-superconductor (SIS) Josephson junction for this purpose. Aluminum is chosen as the superconductor since it is fairly easier and cheaper to fabricate, and the methods

developed here can be applied to fabrication of junctions with other material. And as the insulating layer, in the first experiment aluminum is oxidized and in the second one crystal alumina is deposited.

## 1.2 Overview of the Thesis

In this thesis, we present the fabrication and characterization of Al-$AlO_x$-Al Josephson junctions, and which parameters are important for the quality of the junction; in order to help optimization of Josephson junction fabrication method that produce consistently high quality junctions.

The content of this thesis is as below:

Chapter-1: The goal of the thesis and the theoretical concepts of Josephson junction and the theoretical measurement characteristics of it; theory of superconductivity, Josephson equations, theoretical current-voltage (I-V) and magnetic field characteristics are discussed.

Chapter-2: Experimental methods; two main methods that is used for fabricating Josephson junctions, and instruments and techniques used that is used in this thesis for Josephson junction fabrication. First, the nano-fabrication process is briefly discussed. After that, the fabrications of Al-$AlO_x$-Al Josephson junctions with both oxidation and alumina deposition methods are presented. Finally, the technique used for electrical and magnetic characterization of the device is discussed.

Chapter-3: The results of characterization for both type of junctions is presented; in addition, discussion on the results and the parameters that may have affected the quality of the devices is presented.

Chapter-4: The conclusion and what can be/should be done in order to advance the study as future work is discussed.

## 1.3 Theory of Josephson Junction

The first step is to understand Josephson junctions and the Josephson effect. To achieve this objective, first superconductivity and weak superconductivity which are main concepts for understanding the Josephson effect will be introduced. Then Josephson junction and the Josephson effect will be discussed; Josephson equations are derived.

### 1.3.1 Superconductivity

Superconductivity is the phenomenon that certain conductors have zero electrical resistance (or infinite conductivity) below a certain temperature called critical temperature [3][4]. It was first discovered by in 1911 by H. Kamerlingh Onnes [5]. Onnes demonstrated that at around 4.2 K, resistivity of mercury suddenly dropped to unmeasurable values. In order to confirm that the resistance becomes zero, persistent current experiments conducted by numerous scientist including Onnes himself, which confirmed the superconductivity.

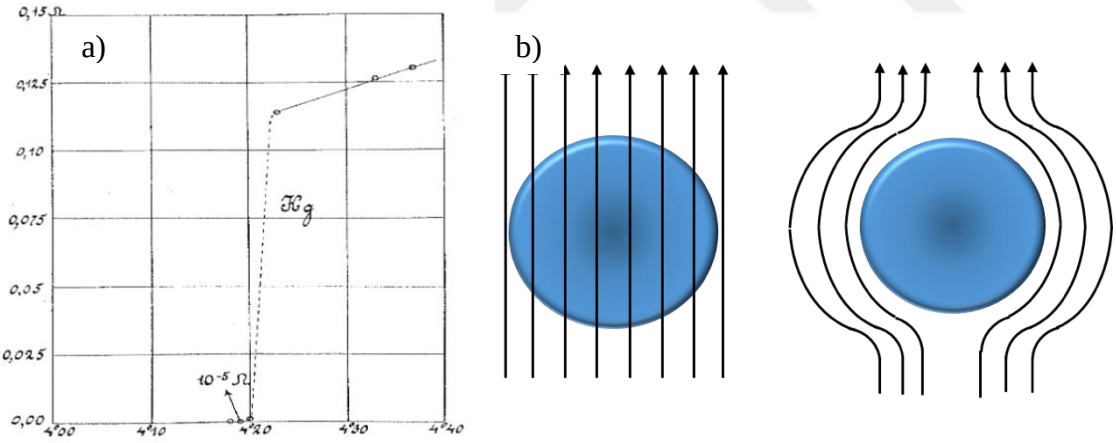


Figure 1.1: Superconducting behavior. a) experimental R-T curve of mercury, showing superconductive behavior (reprinted from Ref. [6]). b) illustration of Meissner effect.

Another important feature of a superconductor is perfect diamagnetism [7]. When a magnetic field is applied to a superconductor, the field cannot penetrate through the superconductor. In addition, when a magnetic field applied to a superconductor when it is in normal regime, as the temperature decreases below $T_c$ and the conductor becomes

superconductive, the field is expelled from the conductor. This phenomenon is called the Meissner effect [4]. According to the Meissner effect, superconductivity will break when a magnetic field higher than a certain field called thermodynamic critical field ($H_c$).

Initially, superconductivity was described as macroscopic quantum system. In this scheme, electrons are assumed to condense to the same quantum state and can be described with a macroscopic wave function [8]:

$$\psi = \rho^{1/2}\, e^{i\varphi} \tag{1-1}$$

Where $\psi$ is the macroscopic wave function, $\rho$ represents the density of electrons in the macro states $|S\rangle$ and $\varphi$ represents the phase common to all of them; $\rho$ is given as:

$$\rho = \langle S|\psi^*\psi|S\rangle = |\psi|^2 \tag{1-2}$$

Later on, superconductivity was formulated by BCS theory as a microscopic quantum system. According to this theory, in the presence of Fermi sea, electrons with equal and opposite momentum and spin attract each other and form pairs called Cooper pairs [9]. Such pairs occupy a slightly lower energy level than other single electrons. Considering both approach. Current density of a superconductor can be written as [8]:

$$\boldsymbol{J} = \rho\, \frac{e}{m}\left(\hbar \nabla\varphi - \frac{2e}{c}\boldsymbol{A}\right) \tag{1-3}$$

Where $\boldsymbol{A}$ is the vector potential, $c$ is the speed of light. The important implication of this relation is that current density depends on the phase value. This will be important when we discuss tunneling in coupled superconductors. In addition, the time evolution of the wave function can be represented with the Schrödinger equation.

$$i\hbar\, \frac{\partial\psi}{\partial t} = E\psi \tag{1-4}$$

Where $E$ is equal to twice the chemical potential.

One last question is whether there is a critical current or not. When a current is high enough to generate a magnetic field higher than $H_c$, then the superconductor will switch to the normal phase [4]. However, this current is on the order of "mA" for a superconductor with the dimensions of our devices and is much higher than the expected critical current (on the order of "μA").

To sum up, certain conductors become superconducting below a critical temperature and a critical field. These are important phenomena to understand and characterize the Josephson junctions. Although we can introduce a critical current, it is negligible for our purpose of characterizing a junction since it is significantly high.

The behavior of a superconductor under magnetic field is explained by London theory [6]. One important result of this theory is the London penetration depth. According to the theory, when a magnetic field is applied to a superconductor, the magnetic field will penetrate the superconductor up to the London penetration depth given as:

$$\lambda_L = \sqrt{\frac{mc^2}{4\pi ne^2}} \tag{1-5}$$

Typical value range for London penetration depth is 50 to 100 nm. For aluminum, the London penetration depth is 51.6 nm [8].

### 1.3.2 Weak Superconductivity

Consider two independent superconductors. In this case, their phase will change independent of each other since they have no interaction. However, if two superconductors are brought to close proximity and separated by a non-superconducting barrier, electrons will start tunneling from one to the other. If the distance between the superconductors is thin enough, not only single electrons but also Cooper paired electrons commence tunneling. In this situation, phase change in such superconductors are no longer independent. As a result, such system behaves like a single superconductor and can be described as one. This phenomenon is called “weak superconductivity” [8][10].

### 1.3.3 Josephson Effect and Josephson Junction

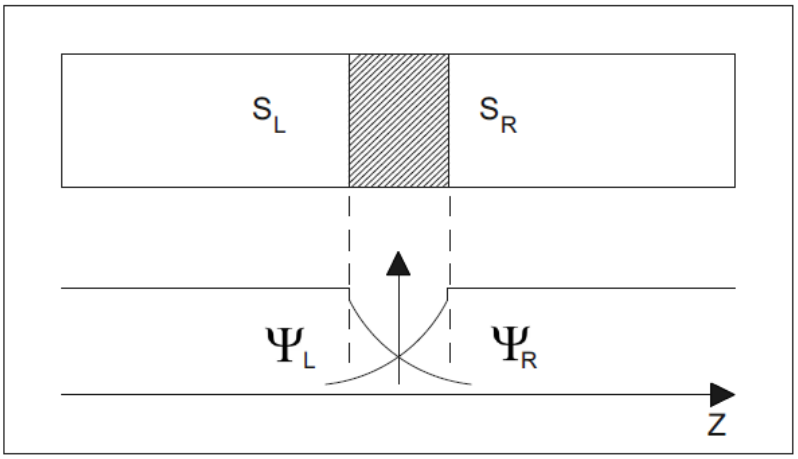


Figure 1.2: Josephson junction. 2 superconductors coupled by a very thin insulating layer.

Josephson effect is first demonstrated and explained by Brian D. Josephson in 1962 [11]. As mentioned in the preceding sections, this phenomenon is the tunneling of cooper pairs between two superconductors when two superconductors in close proximity is separated by a thin barrier that forms a weak link, Cooper pairs tunnel through both superconductors back and forth, even in the absence of an applied voltage [3][11]. The device in which this phenomenon is observed is called Josephson junction and it is fabricated by two layers of superconductor sandwiching a non-superconductor. In this thesis, an insulating layer is used.

Consider the Josephson junction given in figure 1-2 above. Each superconductor will have a wavefunction $\psi_R$ and $\psi_L$, and quantum states $|R\rangle$ and $|L\rangle$ respectively. The density of electrons of each superconductor is given as [8]:

$$\rho_R = \langle R|{\psi_R}^*\psi_R|R\rangle = |\psi_R|^2, \rho_L = \langle L|{\psi_L}^*\psi_L|L\rangle = |\psi_L|^2 \quad (1\text{-}6)$$

Since the superconductors are coupled by a weak link, thus forming a weak superconductor, wavefunctions of the superconductors can be combined and a wave equation for a single superconductor can be written as:

$$|\psi\rangle = \psi_R|R\rangle + \psi_L|L\rangle \quad (1\text{-}7)$$

To find the time evolution of this system, we have to solve the Schrödinger equation:

$$i\hbar\,\frac{\partial|\psi\rangle}{\partial t} = H|\psi\rangle \tag{1-8}$$

Where $H$ is the Hamiltonian of the system. The Hamiltonian is the combination of the Hamiltonian of the right superconductor, the left superconductor, and the tunneling Hamiltonian which represents the interaction between both superconductors. The Hamiltonian is given as:

$$H = H_R + H_L + H_T \tag{1-9.a}$$

$$H_R = E_R|R\rangle\langle R| \tag{1-9.b}$$

$$H_L = E_L|L\rangle\langle L| \tag{1-9.c}$$

$$H_T = K[|L\rangle\langle R| + |R\rangle\langle L|] \tag{1-9.d}$$

Where $E_R$ and $E_L$ are the ground energy states of each superconductors and $K$ is the coupling amplitude and depends on the junction structure.

Writing equation 1-6 for both superconductors separately will give:

$$i\hbar\,\frac{\partial|L\rangle}{\partial t} = E_L\psi_L + K\psi_L \tag{1-10.a}$$

$$i\hbar\,\frac{\partial|R\rangle}{\partial t} = E_R\psi_R + K\psi_R \tag{1-10.b}$$

Where $E_R = 2\mu_R$ and $E_L = 2\mu_L$;.and $\mu_R$ and $\mu_L$ are the chemical potentials. If we consider a DC voltage applied to the junction with the value $V$, the chemical potentials will shift with the amount $eV$. And taking the middle point of the junction as the zero point, we can write $\mu_R = -eV$ and $\mu_L = eV$. Considering this, and replacing wave functions left and right with equation 1-1, we have:

$$\frac{\partial\rho_L}{\partial t} = \frac{2}{\hbar}K\sqrt{\rho_L\rho_R}\,\sin(\varphi_L - \varphi_R) \tag{1-11.a}$$

$$\frac{\partial\rho_R}{\partial t} = -\frac{2}{\hbar}K\sqrt{\rho_L\rho_R}\,\sin(\varphi_L - \varphi_R) \tag{1-11.b}$$

$$\frac{\partial\varphi_L}{\partial t} = \frac{K}{\hbar}\sqrt{\frac{\rho_L}{\rho_R}}\,\cos(\varphi_L - \varphi_R) + \frac{eV}{\hbar} \tag{1-11.c}$$

$$\frac{\partial\varphi_L}{\partial t} = \frac{K}{\hbar}\sqrt{\frac{\rho_L}{\rho_R}}\,\cos(\varphi_L - \varphi_R) - \frac{eV}{\hbar} \tag{1-11.d}$$

From equations 1-11.c and 1-11.d we derive the relation for the phase difference:

$$\frac{\partial \varphi}{\partial t} = \frac{2eV}{\hbar} \tag{1-12}$$

Where $\varphi = \varphi_L - \varphi_R$.

The current density is then $J = \frac{\partial \rho_L}{\partial t} = -\frac{\partial \rho_R}{\partial t}$ where $\rho_L$ and $\rho_R$ are the densities of electron for the superconductors respectively. Thus, from equations 1-10.a and 1-10.b, assuming $\rho_L = \rho_L = \rho$, we can derive the current density. Besides, by integrating equation-11.b we find $\varphi = \varphi_0 + \frac{2eV}{\hbar} t$. By doing the derivation and inserting the term for $\varphi$, we get the following equations for the current density:

$$J = J_C \sin(\varphi);\ J_C = \frac{2K}{\hbar \rho} \tag{1-13.a}$$

$$J = J_C \sin(\varphi_0 + \frac{2eV}{\hbar} t) \tag{1-13.b}$$

Or equivalently:

$$I = I_C \sin(\varphi) \tag{1-13.c}$$

$$I = I_C \sin(\varphi_0 + \frac{2eV}{\hbar} t) \tag{1-13.d}$$

These are the Josephson equations and describe DC and AC Josephson effects.

When the potential across the junction is zero, $\varphi$ is constant. Looking at equations 1-13.a and 1-13.c it is clear that in this case, a current density with the maximum value $J_C$ can flow across the junction. This equation also suggests that a current will flow through the junction even in the absence of a potential. This phenomenon is called the DC Josephson effect.

Equations 1-13.b and 1-13.d indicates that when a potential with a constant value other than zero is applied to the junction, an AC current density will flow through the junction with the maximum amplitude $J_C$ (or an AC current with maximum amplitude $I_C$).

## 1.4 Theoretical Characterization of Josephson Junction

Now the question is, when we fabricate a Josephson junction, how can we understand whether it is really a junction; or more precisely, whether it is a Josephson junction and what type of junction are we dealing with. What is needed to be done to make sense of measurements is to estimate the theoretical characteristics of the junctions and compare them with the results of the measurements in order to do a concrete characterization.

In this part, the theoretical I-V characteristics of a Josephson junction and the classifications of such junctions based on their I-V characteristics and theoretical magnetic field effects will be discussed. We will focus on the DC characteristics of a junction. AC characterization is beyond the scope of this thesis.

### 1.4.1 I-V Characteristics of an SIS Josephson Junction

In the I-V characteristics of a normal metal, a linear curve is observed; and based on the equation 1-13.c, it is clear that when in the superconducting phase, an I-V curve with zero voltage will be observed while the current will be varying within the critical current. When the current is higher than the critical current, the junction will behave like a normal conductor. Thus, a general I-V characteristics of a Josephson junction will be as such: voltage will be zero when the current is within the critical current, otherwise it will be linear. A general I-V curve of a junction is shown in figure 1-3.

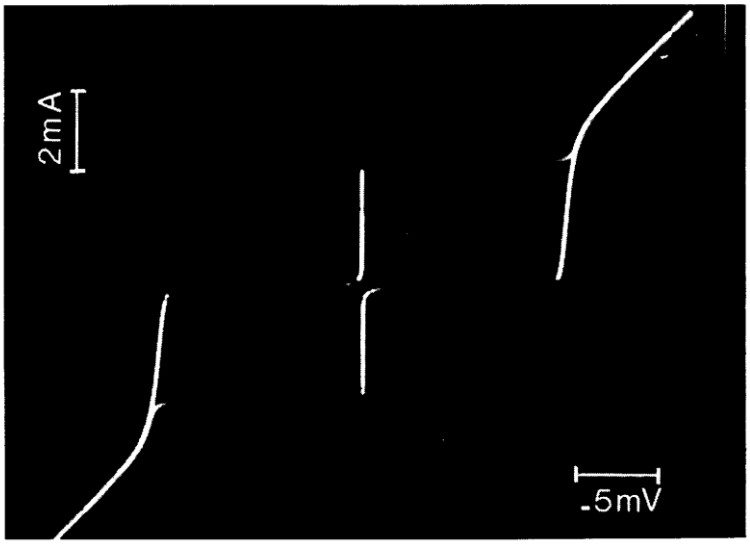


Figure 1.3: I-V characteristics of a Josephson junction (reprinted from Ref. [8], with the permission of Wiley Books).

#### 1.4.1.1 Critical Current of a Junction

Normally, critical current depends on the area of the junction [4]. However, an invariant quantity involving the critical current has been described by the Ambegaokar-Baratoff formula [12]:

$$I_C R_n = \frac{\pi \Delta}{2e} \tanh\left(\frac{\Delta}{2kT}\right) \tag{1-14}$$

Where $R_n$ is the resistance of the junction when both superconductors are in normal state, $k$ is the Boltzmann constant, $T$ is the temperature, $e$ is the charge of an electron and $\Delta$ is the energy gap. The energy gap of aluminum at $T = 0$ is 3.4 μeV [13].

Most of the measurements in this thesis are conducted at $T \sim 20\ mK$, and $\tanh\left(\frac{\Delta}{2kT}\right)$ will converge to 1 for such low temperature values. Therefore, equation 1-14 can be approximated as [4]:

$$I_C R_n = \frac{\pi \Delta(0)}{2e} \tag{1-15}$$

This formula implies that $I_C R_n$ is an invariant quantity and independent of the geometry of the junction [4] which makes sense because $I_c$ and $R_n$ normally scale with junction size

linearly and inversely respectively so their product is expected to be a constant. This formula provides a convenient estimation of the critical current of a junction. Using the characteristics of a superconductor in its normal state from the I-V curve, $R_n$ can be calculated; and inserting this value to the formula critical current can be estimated, irrespective of the geometry of the junction.

#### 1.4.1.2 RCSJ Model

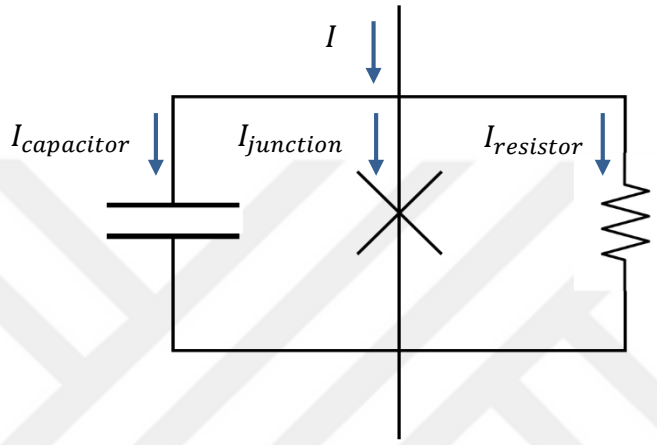


Figure 1.4: RCSJ model representation. An ideal Josephson junction is shunted by a capacitor and a resistor due to the capacitance and resistance of the superconductors and insulating layer.

The equations in the previous parts belong to an ideal Josephson junction. However, in reality there will be other effects and impurities affecting the junction, such as the capacitance or the resistance due to the superconductors or the insulator. Thus, a more realistic and practical model is required to characterize a junction.

For this purpose, a model called resistive capacitive shunted junction (RCSJ) model is developed [14][15]. This model gives an equivalent circuit of a junction; it consists of an ideal junction shunted by a capacitance and a resistance as shown in figure 1.4. In a Josephson junction, not only Cooper pairs but also single electrons commence tunneling. Single electron tunneling is mostly dependent on the voltage applied. And the resistance in this model represents the dissipations of such current, and the capacitance term represents the shunt capacitance between the superconductors.

Assume that the RCSJ circuit is connected to a DC current source. Using the Kirchoff law, the total current in the circuit is [8][16]:

$$I = I_{junction} + I_{capacitor} + I_{resistor} \tag{1-16.a}$$

$$I = I_C \sin(\varphi) + \frac{V}{R} + C\frac{dV}{dt} \tag{1-16.b}$$

Inserting equation 1-12 into equation 1-16.b:

$$I = I_C \sin(\varphi) + \frac{1}{R}\frac{\hbar}{2e}\frac{d\varphi}{dt} + C\frac{\hbar}{2e}\frac{d^2\varphi}{d^2t} \tag{1-17.a}$$

$$\frac{I}{I_C} = \sin(\varphi) + \frac{1}{I_C R}\frac{\hbar}{2e}\frac{d\varphi}{dt} + C\frac{\hbar}{I_C 2e}\frac{d^2\varphi}{d^2t} \tag{1-17.b}$$

For convenience, let us define the dimensionless variables:

$$\tau = w_j t;\ w_j = \sqrt{\frac{2e}{\hbar}\frac{I_C}{C}};\ \beta_j = \frac{1}{w_j}\frac{1}{RC} \tag{1-18}$$

Inserting these into equation 1-17.b:

$$\frac{I}{I_C} = \frac{d^2\varphi}{d^2\tau} + \beta_j\frac{d\varphi}{d\tau} + \sin(\varphi) \tag{1-19}$$

Where $w_j$ is called plasma frequency, and $\beta_j = \frac{1}{\sqrt{B_C}}$ and $B_C$ is the Stewart-McCumber parameter [14][15]. $\beta_j$ is the damping parameter of the junction.

If we insert the Josephson energy $E_j = \frac{\hbar}{2e}I_C$, which is the energy stored in the junction due to supercurrent flow [4], into equation 1-17.b by substituting $I_C$, we get:

$$\frac{I}{E_j}\frac{\hbar}{2e} = \sin(\varphi) + \frac{1}{R}\frac{1}{E_j}\left(\frac{\hbar}{2e}\right)^2\frac{d\varphi}{dt} + C\frac{1}{E_j}\left(\frac{\hbar}{2e}\right)^2\frac{d^2\varphi}{d^2t} \tag{1-20.a}$$

$$C\left(\frac{\hbar}{2e}\right)^2\frac{d^2\varphi}{d^2t} + \frac{1}{R}\left(\frac{\hbar}{2e}\right)^2\frac{d\varphi}{dt} + E_j\sin(\varphi) - I\frac{\hbar}{2e} = 0 \tag{1-20.b}$$

$$C\left(\frac{\hbar}{2e}\right)^2\frac{d^2\varphi}{d^2t} + \frac{1}{R}\left(\frac{\hbar}{2e}\right)^2\frac{d\varphi}{dt} + \frac{d}{d\varphi}\left(-E_j\cos(\varphi) - I\frac{\hbar}{2e}\varphi\right) = 0 \tag{1-20.c}$$

If we look at the equation 1-20.c, we can see that it is like a force equation of a mechanical system. It is analogous to a mechanical system in which a particle with a mass $C\left(\frac{\hbar}{2e}\right)^2$ moving along the $\varphi$ axis with an effective potential energy [4]:

$$U(\varphi) = -E_j \cos(\varphi) - I\frac{\hbar}{2e}\varphi \qquad \text{(1-21.a)}$$

Or:

$$U(\varphi) = -E_j \cos(\varphi) - \frac{I}{I_C}\varphi \qquad \text{(1-21.b)}$$

The middle term in the equation is drag force.

This potential representation of Josephson junction is called tilted-washboard potential and the plot of equation-20 is given in figure 1-5.

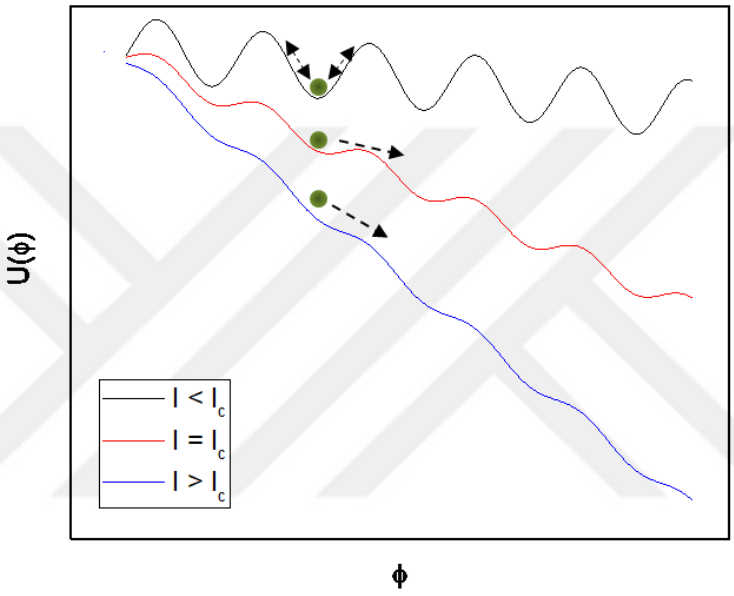


Figure 1.5: Tilted washboard potential model of a junction.

Looking at the equation and the figure, when $I < I_C$ there are local minima and thus equilibrium points. Using the mechanical analogy, when the particle is at one of the minima, it is in equilibrium and will stay there. The particle being at equilibrium means that $\varphi$ will be constant in average. Since the voltage is proportional to the derivative of the phase difference $\varphi$, and since it is constant, $\frac{d\varphi}{dt}$ and thus $V$ will be zero. This means that when we apply current to the junction smaller than $|I_C|$ we will read a zero voltage.

When $I = I_C$, the minima will become flat and the washboard potential convert into horizontal steps in an inclined potential. Thus there will be no local minima and no stable equilibrium point. When $I > I_C$, the potential will be continuous inclined curve.

Therefore, when $I \geq I_C$, junction voltage will no longer be zero and increase with the current applied.

Another important result can be derived from the RCSJ model is the uncertainty principle of the phase difference and the charge. Although this subject is beyond the scope of this thesis, it is important for the future work and the application of Josephson junction.

From quantum mechanics uncertainty principle states:

$$\Delta P . \Delta x \approx \hbar$$

Using the mechanical analogy we can replace $x$ with $\varphi$ and then the momentum is:

$$P = M\dot{\varphi} = C\left(\frac{\hbar}{2e}\right)^2 \dot{\varphi} = \frac{\hbar}{2e} CV = \frac{\hbar}{2e} Q$$

Where $Q$ is the charge. If we insert these to the uncertainty equation, we get:

$$\Delta \frac{\hbar}{2e} Q . \Delta \varphi \approx \hbar$$

$$\Delta Q . \Delta \varphi \approx 2e$$

$$\Delta n . \Delta \varphi \approx 1 \qquad (1\text{-}22)$$

Where n represents the number of Cooper pairs. This relation also applies to an isolated superconductor, in which $n$ will be fixed and thus $\varphi$ will be undefined [8]. But in a junction, we can fix any of the parameters. When the charging energy $E_c = \frac{e^2}{2C}$ of a junction due to the capacitance of the superconductors is much smaller than the Josephson energy $E_c \ll E_j$, this means that charges will be fixed and the phase will be undefined, thereby providing a phase coherence. On the other hand, when $E_c \gg E_j$ there will be charge coherence. The former is the phenomenon used to make flux qubit whereas the latter is for charge qubit.

#### 1.4.1.3 Overdamped Junction

If the capacitance is small and thus $\beta_j \gg 1$, the damping effect will be much higher than the inertia and will dominate it [4]. Considering the tilted washboard potential, when $I \geq I_C$, the washboard potential will be tilted and minima will be flattened, and the particle will move along the $\varphi$ axis. And when we reform the washboard potential, the local minima will reform again and due to high damping, the particle will immediately settle at one of the minima and will become stable. This means that when $I \geq I_C$ and so the junction is not in the superconducting state, and we decrease the current again back to $I \leq I_C$, the potential will immediately back come back to zero, exactly at $I = I_C$. Therefore, there will be no hysteresis in the junction. This kind of junction is called Overdamped Junction.

When $\beta_j \gg 1$, second derivative term can be neglected in equation 1-19 can be neglected and thus equation 1-19 reduces to first degree ordinary differential equation:

$$\frac{d\varphi}{d\tau} = \frac{1}{\beta_j}\left(\frac{I}{I_C} - \sin(\varphi)\right) \tag{1-23}$$

Since $\frac{\partial\varphi}{\partial t} = \frac{2eV}{\hbar}$, we can find the time average voltage from equation 1-23 as:

$$V = R\sqrt{\left(I^2 - {I_C}^2\right)} \tag{1-24}$$

This suggests that when $I < I_C$ the voltage is zero and otherwise it is as in equation 1-24.

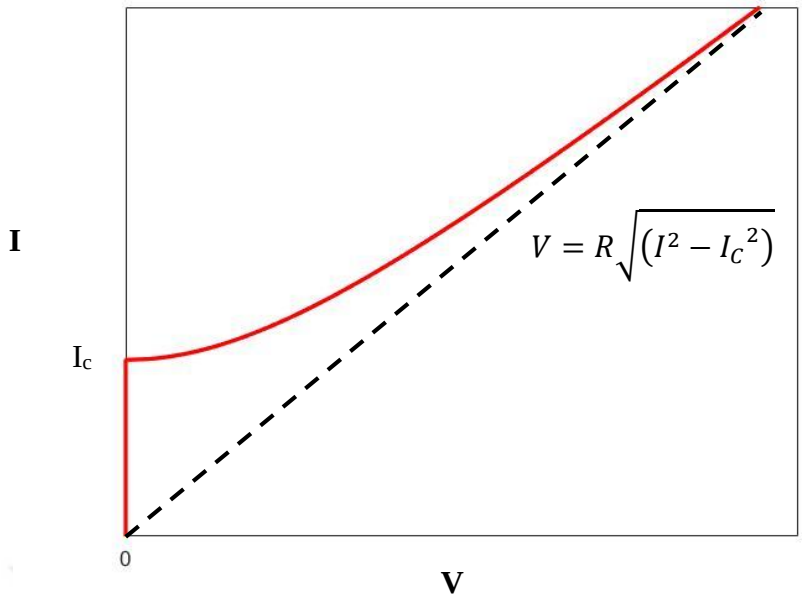


Figure 1.6: I-V behavior of an overdamped junction. When $I < I_C$, the voltage is zero; otherwise, it is $V = R\sqrt{(I^2 - I_C{}^2)}$

#### 1.4.1.4 Underdamped Junction

When the capacitance is high and so $\beta_j \ll 1$, the damping force will be very small. Since $mass = C\left(\frac{\hbar}{2e}\right)^2$ the inertia will be large. Consequently, the inertia will dominate the damping force. Considering the tilted washboard potential again, when $I \geq I_C$, the particle will move along the $\varphi$ axis which means the potential will not be zero. It will be equal to $V = IR_n$. But when we reform the washboard potential, due to low damping and high inertia, more time and effort will be required to stop the particle at a local minimum. This imply that when we decrease the current below the critical current, the junction will not return immediately to the superconducting phase. There will still be potential for some time and it will return to zero at a current value less than the critical current. This returning current is called "retrapping current" and it is given as [4]:

$$I_r \approx \frac{4I_C\beta_j}{\pi} \tag{1-25}$$

Therefore, there will be hysteresis in the junction. This kind of junction is called Overdamped Junction.

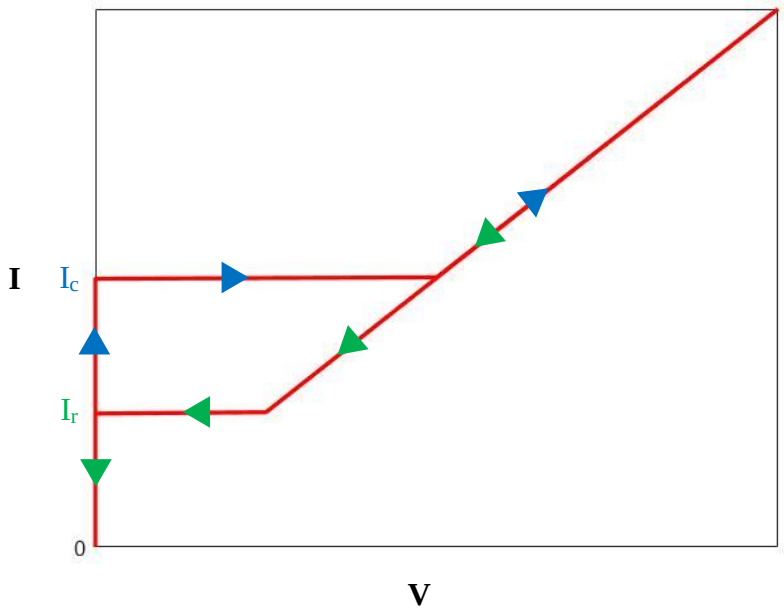


Figure 1.7: Hysteretic behavior of an underdamped junction. When $I < I_C$, the voltage is zero. When $I \geq I_C$, it is $V = IR_n$. While sweeping the current back to zero, the junction does not switch back to the superconducting state immediately at $I = I_C$; instead, it will switch back at $I = I_r$.

#### 1.4.1.5 Effects of Thermal Fluctuations

So far in this part, we discussed I-V characteristics without considering thermal fluctuations. Thermal fluctuations are the deviations in the current from the mean value d. Thermal fluctuations will be important when $2E_j$ is significantly larger than $kT$ [4]. When the temperature is smaller than the critical temperature:

$$\frac{2E_j}{kT} = \frac{R_Q}{R_n}\frac{T_c}{T} \tag{1-26}$$

Where $R_Q = \frac{h}{4e^2} = 6.453\ \Omega$ is the quantum resistance. Considering the equation above, when $R_Q > R_N$ effects of thermal fluctuations are significant down to $\frac{R_Q}{R_n} \approx \frac{T}{T_c}$, otherwise they will be important near $T_c$.

#### 1.4.1.6 Effects in Underdamped Junction

One effect due to thermal fluctuations occurs is the premature switching [4][17]. In this phenomenon, when we scan the current value through the critical current, there is a probability of switching to the normal state before the current reaches to the critical current due to thermal activation. Therefore, if we sweep current repetitively through a junction in the presence of thermal activation, we might see multiple critical current points; or more precisely, we may see switching occur at various current values.

Thermal fluctuations may also effect the retrapping current. Retrapping current is proportional to the damping. If we consider the additional damping due to the thermal activations, retrapping current may increase. Consequently, we may observe a bigger retrapping current than the one without fluctuations.

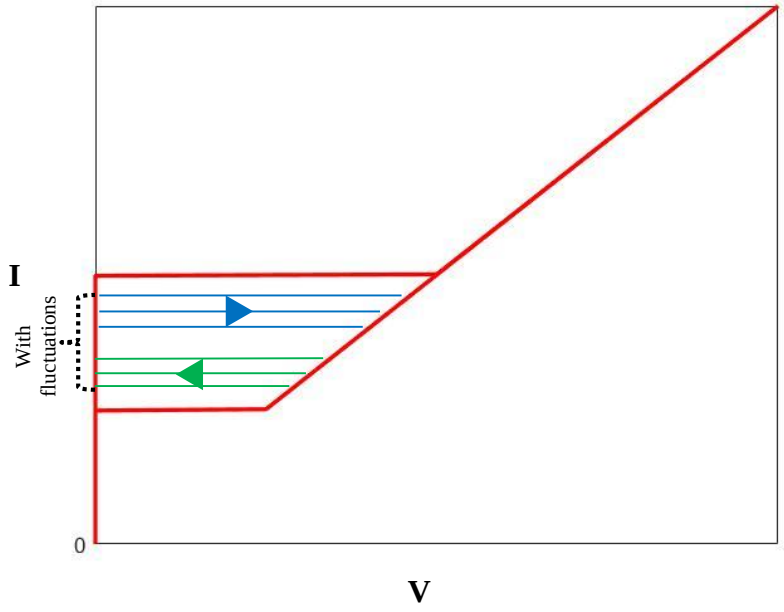


Figure 1.8: Effects of thermal fluctuations in critical and retrapping currents. Thermal fluctuations may decrease the critical current value (represented with blue lines) whereas it may increase the retrapping current value (represented with green lines).

### 1.4.2 Magnetic Field Effects

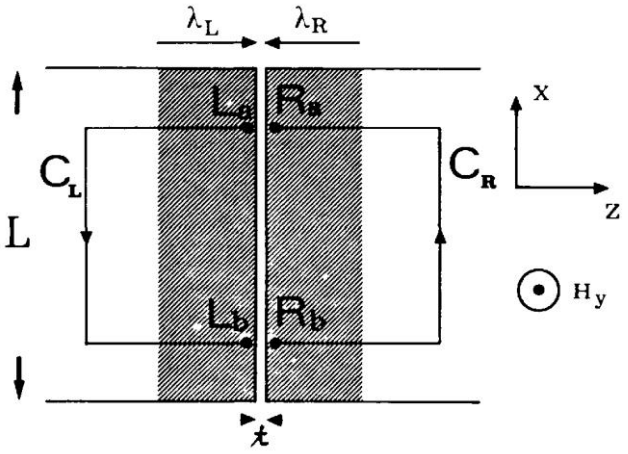


Figure 1.9: Representation of a junction under a magnetic field perpendicular to the direction of current flow (reprinted from Ref. [8], with the permission of Wiley Books). $\lambda_L$ and $\lambda_R$ are London penetration depths of superconductors, L is the width of the junction parallel to the magnetic field, and t is the insulating layer thickness.

If we apply a magnetic field to a junction, the phase of the particles will be affected by the field. Thus we need to derive an equation for Josephson current which includes the magnetic field term. In order to do that, we must find the phase difference in terms of the magnetic field.

Let us now consider the figure above. Assume that the magnetic field is in the y direction and thus parallel to the insulating layer (or perpendicular to the current flow). Since $\nabla x\boldsymbol{A} = \boldsymbol{H}$ where $\boldsymbol{A}$ is the vector potential and $\boldsymbol{H}$ is the magnetic field, and assuming that the thickness of the superconductors are bigger than the London penetration depth $\lambda_L$, we can define the contour shown in the figure outside the penetration depth.

From equation 1-3, we have [4]:

$$\nabla\varphi = \frac{2e}{\hbar c}\left(\frac{mc}{2\rho e^2}\boldsymbol{J} + \boldsymbol{A}\right) \tag{1-27}$$

If we take the integrals of above equation along the curves we get:

$$\varphi_{Ra}(x) - \varphi_{Rb}(x+dx) = \frac{2e}{\hbar c}\int_{C_R}\left(\frac{mc}{2\rho e^2}\boldsymbol{J} + \boldsymbol{A}\right)\boldsymbol{dl} \tag{1-28.a}$$

$$\varphi_{Lb}(x+dx) - \varphi_{La}(x) = \frac{2e}{\hbar c}\int_{C_L}\left(\frac{mc}{2\rho e^2}\boldsymbol{J} + \boldsymbol{A}\right)\boldsymbol{dl} \tag{1-28.b}$$

Thus:

$$\varphi(x) - \varphi(x+dx) = [\varphi_{Lb}(x+dx) - \varphi_{Rb}(x+dx)] - [\varphi_{La}(x) - \varphi_{Ra}(x)] \tag{1-29.a}$$

$$\varphi(x) - \varphi(x+dx) = \frac{2e}{\hbar c}\left[\int_{C_R}\left(\frac{mc}{2\rho e^2}\boldsymbol{J} + \boldsymbol{A}\right)\boldsymbol{dl} + \int_{C_L}\left(\frac{mc}{2\rho e^2}\boldsymbol{J} + \boldsymbol{A}\right)\boldsymbol{dl}\right] \tag{1-29.b}$$

If we choose contours perpendicular to $\boldsymbol{J}$, first term of each integral can be neglected. In addition, if we also neglect the barrier thickness we will have:

$$\varphi(x) - \varphi(x+dx) = \frac{2e}{\hbar c}\oint \boldsymbol{A}\boldsymbol{dl} \tag{1-30}$$

From the Stoke's theorem:

$$\oint \boldsymbol{A}\boldsymbol{dl} = \iint (\nabla x\boldsymbol{H})\, dxdz = H(2\lambda_L + t)dx \tag{1-31}$$

Where $t$ is the barrier thickness. Inserting this term into equation 1-30 we have:

$$\varphi(x) - \varphi(x + dx) = \frac{2e}{\hbar c} H[2\lambda_L + t]dx \tag{1-32.a}$$

$$\frac{d\varphi}{dx} = \frac{2e}{\hbar c} H[2\lambda_L + t] \tag{1-32.b}$$

By integrating equation 1-32.b we get:

$$\varphi = \varphi_0 + \frac{2e}{\hbar c} H[2\lambda_L + t]x \tag{1-33}$$

Therefore:

$$J = J_C \sin(\varphi_0 + \frac{2e}{\hbar c} H[2\lambda_L + t]x) \tag{1-34}$$

Equation 1-34 indicates that Josephson current is modulated spatially by the applied magnetic field.

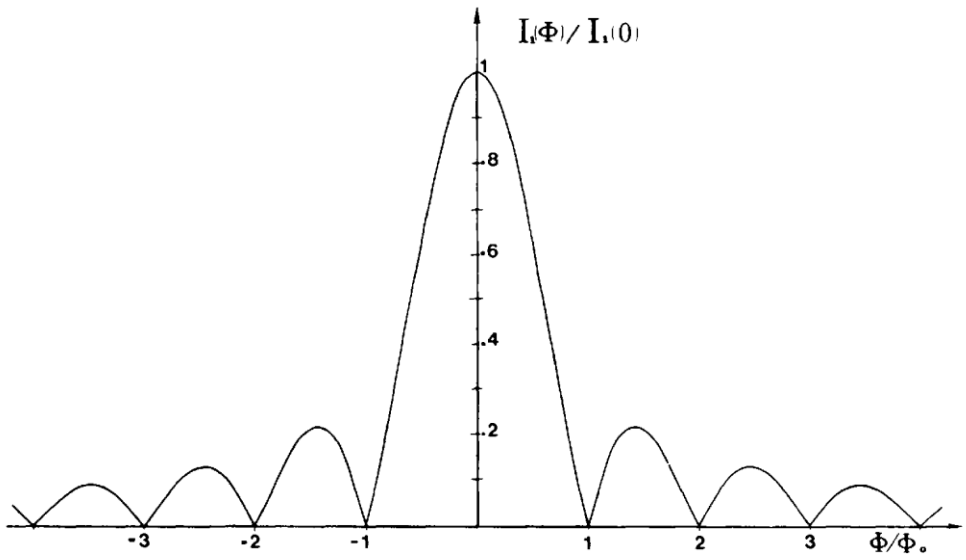


Figure 1.10: Magnetic field-critical current characteristics of a rectangular junction. The pattern indicates a Fraunhofer diffraction pattern (reprinted from Ref. [8], with the permission of Wiley Books).

If we integrate equation 1-34 over the junction area we find the magnetic field dependent critical current as:

$$I_C(H) = I_C(0)\left|\frac{\sin(\pi\frac{\varphi}{\varphi_0})}{\pi\frac{\varphi}{\varphi_0}}\right| \tag{1-35}$$

Where $\varphi = HL[2\lambda_L + t]$, $\varphi_0 = \frac{hc}{2e} = 2.067\ x\ 10^{-15} Wb$ is the flux quantum. This equation suggests that we will have a periodic curve for magnetic field vs. critical current characteristics. This pattern is shown in figure 1-10 and it is called Fraunhofer diffraction pattern [8][18].

Another important phenomenon of the magnetic field is the Josephson penetration depth, which is given as:

$$\lambda_J = \sqrt{\frac{\hbar c^2}{8\pi e J_C d}} \tag{1-36.a}$$

Or in MKS units:

$$\lambda_J = \sqrt{\frac{\hbar}{4e\mu_0 d J_C}} \tag{1-36.b}$$

Where $d = \lambda_L + \lambda_R + t = 2\lambda + t$.

If the transverse dimension of a junction is smaller than the Josephson penetration depth, it is considered as small junction. In this kind of junction self-induced magnetic field due to the current can be neglected and we will mainly get a uniform current distribution. Therefore, we would expect to observe for such junctions the Fraunhofer pattern presented above. On the other hand, if the transverse dimension is smaller, the current will confine to the edges of the junction.

In this thesis, typical transverse dimension is on the order of 100 nm. For aluminum, $\lambda_L = 51.6\,nm$ [8]; and thickness can be neglected since it is on the order of a few nm. Thus $d \approx 100\,nm$. considering the observed $I_C$ values of the junctions in this thesis (presented in "Results and Discussion" chapter), Josephson penetration depth is calculated as $\lambda_J \approx 4\,\mu m$. Since the junction dimensions are much smaller than the penetration depth, they are considered as small junctions.

For small junctions, various Fraunhofer patterns are defined, based on the geometry and the uniformity of the current density. Some of those patterns are briefly discussed in this subsection.

Assuming we have a rectangular junction geometry and uniform current distribution, and equation 1-35 is valid, we will get a pattern as shown in figure 1.10.

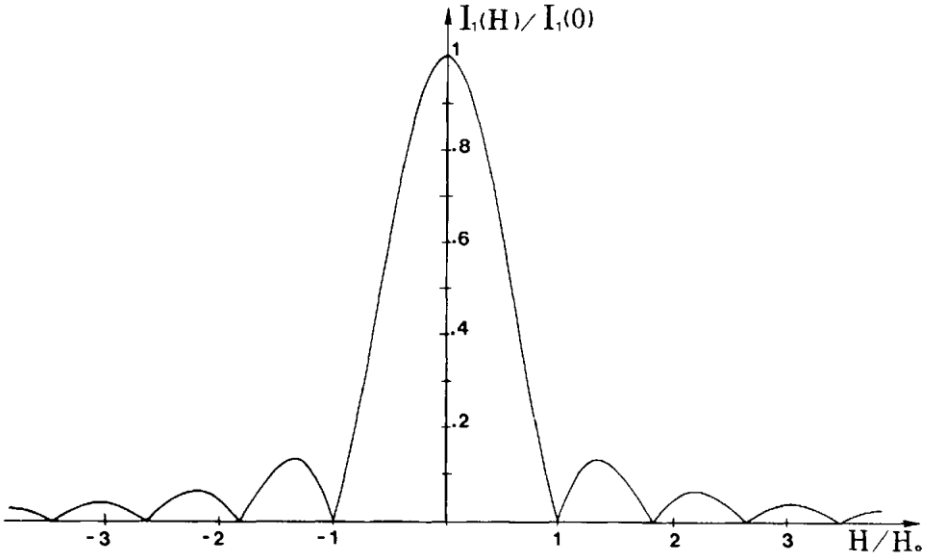


Figure 1.11: Fraunhofer pattern in a circular junction. It can be inferred from the figure that depending on the shape of a junction, Fraunhofer pattern may compress or expand in the x direction. (reprinted from Ref. [8], with the permission of Wiley Books).

As shown in the figure 1.10, at $\frac{H}{H_0} = \frac{\varphi}{\varphi_0} = 1, 2, 3, \ldots$, we will observe the critical current to be zero and superconductivity to be vanished for the rectangular junction. However, for the circular junction we will observe shift in the vanishing points as shown in figure 1.11.

What if the magnetic field is not in the y direction as we assumed and in an arbitrary direction? Assuming that the magnetic field also has x component, we can find the pattern in the presence of such a field. The theoretical results in this case is shown in figure 1.12. It can be seen from the figure that as the angle between the x axis and the direction of the field increase, the pattern shrinks.

Now it is time to discuss the effects of non-uniform current density. Due to the topological impurities such as thickness variations in the insulating layer resulting from the

fabrication processes, the current density might not be uniform. This will result in a different pattern, although it would still be similar.

For more detailed discussion, one can refer to A. Barone (1982).

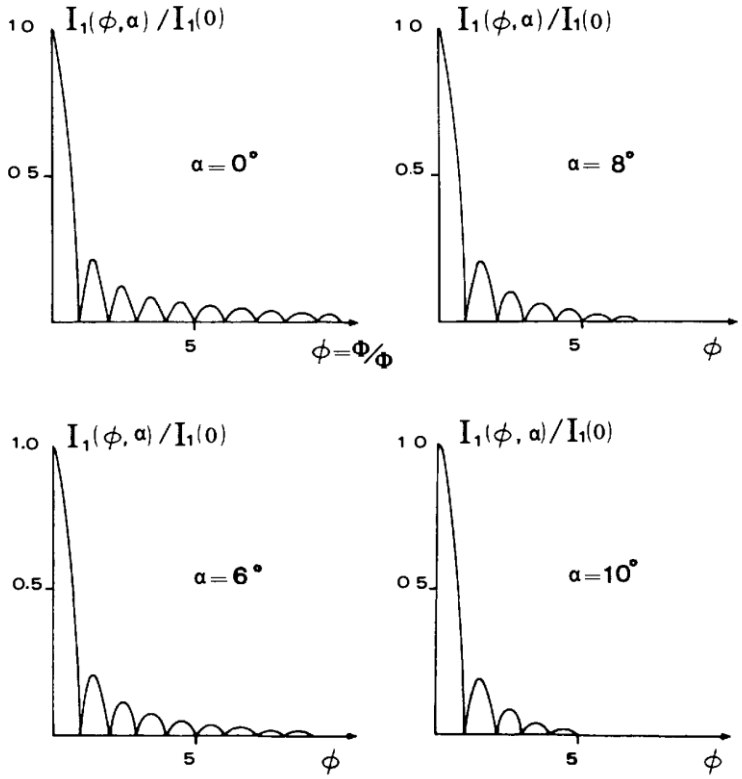


Figure 1.12: Fraunhofer patterns at magnetic field with various angles to x direction (reprinted from Ref. [8], with the permission of Wiley Books).

# 2. EXPERIMENT

In the previous part, the theory and theoretical characteristics of a Josephson junction is discussed. In this part, the fabrication and characterization methods will be discussed; first the fabrication in detail, then the characterization of the samples fabricated.

In this thesis work initially the devices were fabricated using nanofabrication techniques, then they were inspected scanning electron microscopy (SEM) and optical microscopy to determine if the fabrication was successful. Finally, the characterization of the samples was conducted using a dilution refrigerator and electrical measurement instruments.

## 2.1 Fabrication of Josephson Junction

### 2.1.1 A Brief Overview of Nanofabrication Process

The general processes of fabrication are illustrated in figure 2.1. What basically done is to fabricate nano-size circuits. The first step is to design the circuits for which a CAD program called Layout-Editor is used.

Si-$SiO_2$ wafers are used to fabricate the circuits on since high resolution can be achieved on these wafers by EBL, they are commercially available and commonly used in micro-nano fabrication. To pattern the design on the substrate, lithography techniques are used. Crudely speaking, lithography is a method to print pictures or in this case designs on a substrate. First the substrate is coated with a chemical generally referred as “resist” in which the molecules undergoes chemical changes when exposed to UV light or electron beam. The patterns are transferred on the resist via photolithography (UV light) or electron beam lithography (high energy electrons). Then, the substrate is exposed to a chemical referred as “developer”. In this process, light or electron exposed areas of the

coated resist will be removed completely (this refers to a positive resist) and the unexposed regions will remain, thereby generating the design on the substrate.

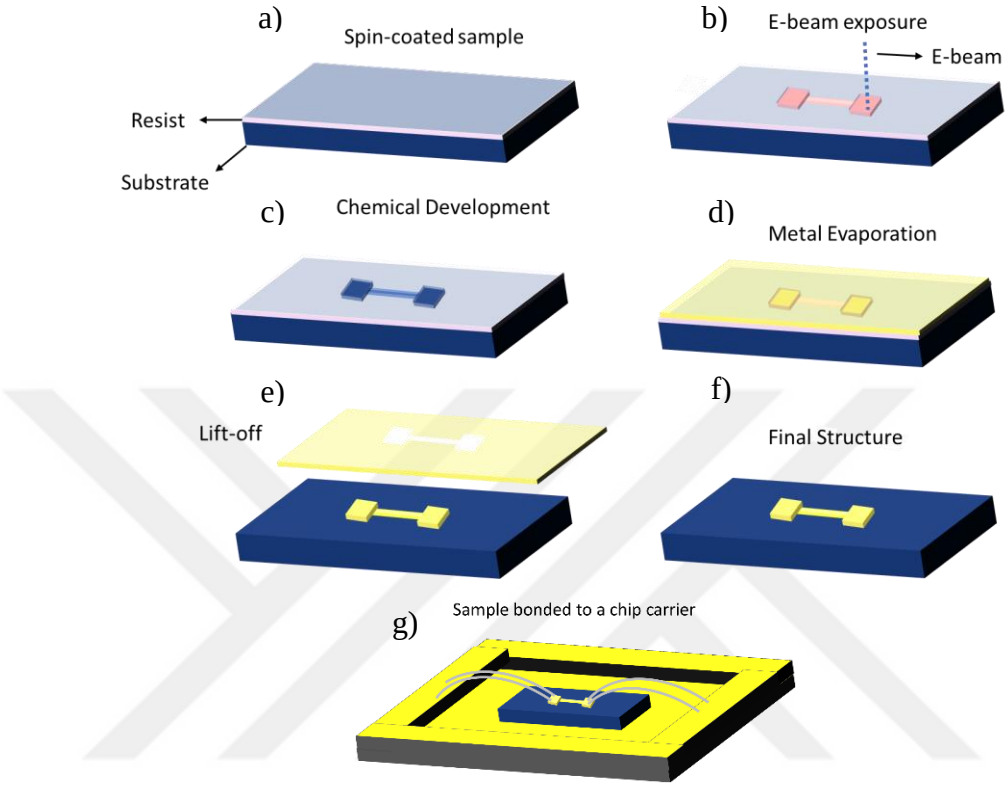


Figure 2.1: Illustration of one type of nanofabrication process called lift-off which is an additive process often used to create metal micro/nano patterns on a substrate. The order of processes is the same as letter marks and the final step (g) is merely to make electrical access to the ~ 0.1 mm size contacts.

Next step is to deposit metal. We use evaporation techniques in which a metal source is heated to temperature where its partial pressure reaches ~$10^{-4}$ mbar, hence starts evaporating at a reasonable rate for coating surfaces. Substrates are loaded into a vacuum chamber with base pressure of < $10^{-5}$ mbar and the metal is coated under vacuum over the whole surface of the substrate.

Following the metal deposition, the excess metal, metal other than our circuit, should be removed from the substrate. Since the excess metal will be on the remaining (undeveloped) resist, removal of the it gets the job done. This process is called “lift off”,

and in this process we put the substrate in acetone for few minutes or longer as needed. The undeveloped resist and together with the metal on it is removed during lift-off.

The final step is to die bond the substrate on a chip carrier and connect the contacts of the circuit to the contact pads of the chip carrier for the purpose of measurement.

Nano-fabrication processes require a clean room since device sizes are small and so even micron sized dust particles in air and other contaminants can easily affect the quality of devices significantly. The fabrication of the devices in this thesis work were conducted in the clean room located at Sabanci University Nanotechnology Research and Application Center (SUNUM).

### 2.1.2 Overview of the Experiment

To fabricate a junction using nanofabrication methods, first the bottom layer aluminum is deposited. Next, the insulating layer is formed. Finally, the top layer aluminum is deposited and junction is formed. In this thesis, two separate methods are used to fabricate Al-AlOx-Al junction. The first one, which is also the most common method, is to form the insulating layer by oxidizing the bottom layer before depositing the top layer. In order to prevent the contamination of the junctions, the depositions and oxidation are conducted in a single evacuation cycle. To achieve this, a method called shadow angle evaporation is used which is explained in section 2.1.2.6 in detail.

*Oxidation Process:* The oxidation process is very important since it determines the quality of a junction. Oxidation is done by exposing the aluminum layer to oxygen gas by filling the evaporation chamber with oxygen.

There are couple of important points with oxidation of aluminum. When exposed to oxygen gas, aluminum reacts with oxygen and a native oxide layer is formed on its surface. Oxidation rate depends on parameters such as oxygen pressure, substrate temperature and exposure time [8][20][21]. Both experimental and computational studies have been conducted on the oxidation process. Such studies suggest that as the oxygen pressure or the substrate temperature, or the exposure time increases, oxidation and thus

the oxide layer thickness increases [8][20][21]. Although some metals are needed to be heated, aluminum can be oxidized at room temperature.

Another important point with aluminum oxidation is that it is self-limiting [8]. As the oxide layer grows on the surface, eventually it blocks the oxygen gas from interacting with the metal. Therefore, when a certain thickness of oxide covers aluminum, there will be no further oxidation and the oxide layer will reach its maximum thickness. This is very useful to obtain a uniform oxide layer; and a high quality junction. A varying thickness profile would result in an inhomogeneity in the current density since the tunneling current is a strong function of the barrier thickness and current flows through the regions where barrier is thinner. The disadvantage of the self-limited oxidation is the long wait time which increases the chance of picking up contamination from the chamber.

Another important point is formation of unintended pinholes through the insulating layer. During the oxidation process, oxygen gas may accumulate at some areas on the metal instead of distributing evenly, resulting in no oxidation thereby creating pinholes. If this happens, two layers of superconductors may be short circuited leading to a poor quality junction. However, it is computationally shown that as the oxidation process continues, these pinholes will be filled [19]. This suggests that oxidation process should not be stopped prematurely and the metal should be exposed to oxygen gas for long enough time. Studies report that average oxide layer thickness for aluminum junctions at room temperature is between 1.5 nm and 2 nm [20][21].

For a good quality junction, a uniform insulating layer without any pinholes is required. Considering the information above, a high pressure and a long exposure time should be used. For this experiment, 1 mbar and 5 mbar oxygen pressure values are used along with 1 hour and 6 hours exposure time respectively.

The theory on the oxidation for thin films are still in development. Even though higher parameters are chosen to maximize oxidation, it is still uncertain whether a uniform layer will form. In addition, thickness of the layer is uncontrollable; the thickness cannot be arbitrarily chosen. Thus, it is assessed that an alternative to oxidation which provides controllable thickness and uniform layer might be more useful. Therefore, we utilized a second method, deposition of aluminum oxide via e-beam evaporation is used to form the insulating layer. However, this requires modifications in the fabrication processes as well as the design. The evaporation chamber (VAKSIS) used for shadow angle

evaporation does not have e-beam evaporation capability and the alternative evaporation chamber we have (Torr evaporator) which has the e-beam capability is not suitable for shadow angle evaporation method. Therefore, an alternative evaporation method is implemented in order to fabricate junctions at once. The method is explained in part 2.1.4.6.

### 2.1.3 Fabrication of Al-$AlO_x$-Al Josephson Junction with Oxidation

In this part, the fabrication process that is used for fabricating Al-$AlO_x$-Al Josephson junction with oxidation will be discussed in detail.

#### 2.1.3.1 Layout Design

The design of the device is illustrated in figure 2.2. Dark areas are the background and red and blue areas belong to the design; they are the areas EBL system will expose with electron beam on the substrate. The color difference is due to the resolution. As discussed in the relevant subsection, resolution value is selected on the EBL software which determines the dot separation (pixel size) and hence the beam current. Since very small structures are needed for the actual device part of the circuit, a fine resolution value is chosen which is represented by another layer (or color) in the design. Since the red regions do not contain small features, it is not necessary to use high resolution. Use of lower resolution allows high beam current and reduces the exposure time.

The square parts designed for the purpose of connecting the device to the chip carrier and are called *bond pads*. Active area of the device is shown in figure 2.2 b). As discussed in the relevant subsection, a specific deposition technique called “shadow angle evaporation” or “Dolan bridge” is used. The separation between the leads are the bridge that is required to form in order to use this method.

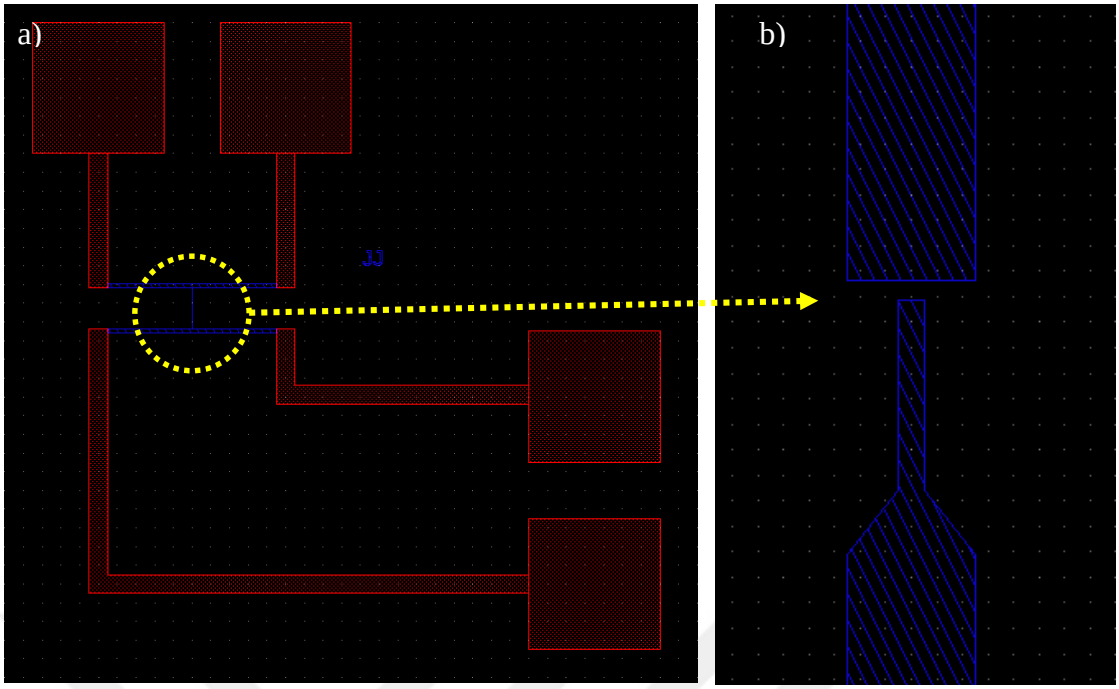


Figure 2.2: Layout design of the junction. a) device and the contacts, b) pattern for the junction.

#### 2.1.3.2 Substrate preparation

As the substrate, 1 cm x 1 cm pieces from Si-$SiO_2$ (285 nm $SiO_x$ grown on 575 μm thick Si) wafers are used. First step is to clean the substrate in order to get rid of the contaminants such as dust or pieces of silicon on the substrate. To achieve this, the silicon pieces are placed inside a glass petri dish filled with acetone for a few minutes; and if necessary, the petri dish is sonicated to achieve better cleanliness. Then, the substrate is placed in another petri dish filled with isopropyl alcohol (IPA) to clean the acetone residue for about 30 seconds. Finally, the substrate is removed from the petri dish and dried by blowing clean nitrogen gas.

#### 2.1.3.3 Coating PMMA on the Substrate

For electron beam lithography most commonly used resist is Polymethyl methacrylate (PMMA). To print the design successfully all over the sample, it is necessary to coat

PMMA with a uniform thickness. An instrument called “spin coater” is used to achieve this, which spins the substrate and the PMMA which is dissolved in an adequate solvent uniformly covers the surface due to centrifugal force.

There are various types of PMMA according to their molecular weights. The thickness of the resist after spin coating is determined by rotation speed as well the concentration of the PMMA used. Molecular weight of PMMA determines its sensitivity to the electron beam, which is used as a parameter when multilayer resist fabrication schemes are utilized.

Electron beam penetrates and scatter through the resist during the EBL process. Depending on the molecular weight of the resist and the spin coating speed, the thickness of the coated PMMA varies. This is important because one can coat two or more layers of PMMA rather than single layer, to achieve more robust deposition or to achieve design goals. Consequently, PMMA thicknesses and EBL dose values should be optimized before EBL processes, in order to print the design precisely (without any feature loss etc.). For this fabrication process, bi- layer PMMA is used. In the bottom layer, a thick layer of PMMA with smaller atomic weight is coated and in the top layer, a much thinner PMMA layer with larger atomic weight is spin coated. This is required to form the bridge for shadow angle evaporation. With the top layer, the bridge will be formed and the bottom layer PMMA under this bridge should be removed completely. The coating process is optimized for this as discussed in the following paragraph.

The resists used as the bottom layer is PMMA/MMA EL11. The aim is to have 700 nm resist thickness for the first layer which acts as the sacrificial/support layer for the top PMMA layer. As the top layer, PMMA 950/A5 is used and achieving 150 nm resist thickness is aimed; this is the layer actual pattern is precisely formed. The coating process is done as follows [21]:

1. Spin coat the substrate with PMMA/MMA EL11 with spin speed 2500 rpm/min for 60 seconds,
2. Bake the substrate at 180 °C for 5 minutes,
3. Spin coat the substrate with PMMA 950/A5 with spin speed 3500 rpm/min for 60 seconds,
4. Bake the substrate at 180 °C for 10 minutes.

This bilayer resist structure can give a wide undercut profile and allow formation of the bridge at the junction area.

#### 2.1.3.4 Patterning with Electron Beam Lithography

Next step is patterning, or drawing the design onto the PMMA coated substrate. EBL is a method to draw the design pattern using electron beam. Vistec EBPG5000+ EBL System located in SUNUM is used for EBL.

Hardware of an EBL system is similar to SEM with an additional feature of having an arbitrarily steerable beam. When the electron beam enters the resist. It starts to scatter and penetrate through the resist. Depending on the electron energy and atomic weight, penetration and scattering volume changes; lighter the weight larger the volume. Therefore, in order to get the optimal penetration and thus optimal patterning, dose value should be optimized. In this fabrication. I used the optimized dose value of 1500 $\mu C/cm^2$ [21].

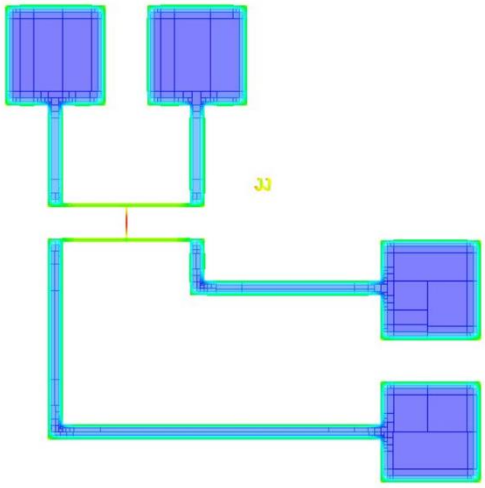

Figure 2.3: Picture of the design after PEC correction for dose using EBL software. Lighter colors represent higher dose values.

Another important point is the proximity effect and its correction. Electron beam will penetrate through the resist and some of it will interact with the substrate, generating backscattered electrons. These electrons may expose the regions of the resist that are not

intended to be exposed, thereby distorting the pattern. To prevent this from happening, an additional software feature called proximity effect correction (PEC) is utilized. Using the software of the instrument, entering substrate and resist type, software automatically alters the dose value at different parts of a pattern with certain shape and size to get optimum dosing.

#### 2.1.3.5 Developing the Patterned Substrate

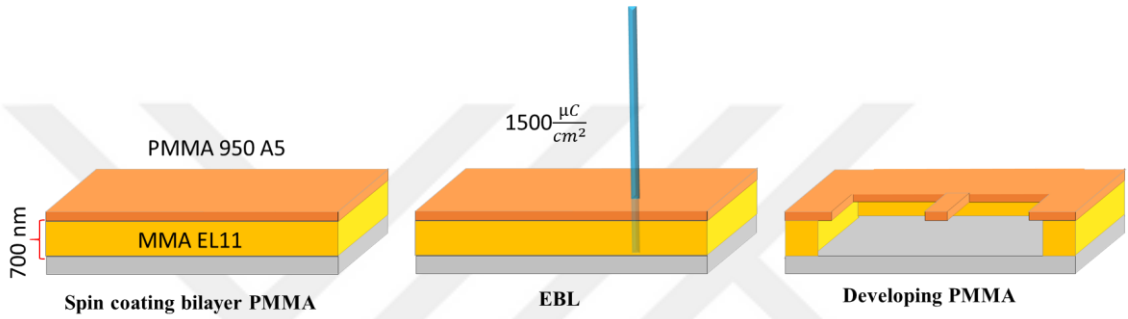


Figure 2.4: Illustration of development process. The substrate coated bilayer PMMA and patterned with EBL using the dose value shown in figure, finally developed and the bridge is formed for shadow angle evaporation.

Once the EBL exposure is finished, PMMA in the exposed regions needs to be dissolved and removed. When exposed with electron beam, the chemistry of PMMA will change and can be removed by dipping in a solvent called methyl isobutyl ketone (MIBK) or a mixture of MIBK and IPA. This process is called “developing”.

Similar to the dosing, developing process should also be optimized; if we use higher concentration of MIBK or develop for longer than needed, the PMMA will be overdeveloped and edges will be rounded or even the patterns may be lost. On the contrary, if we develop for too short time or use too dilute MIBK, PMMA will be underdeveloped and will leave residues on the surface.

The development recipe used as follows [21]:

1. Dip the substrate in 1:2 MIBK:IPA for 2 minutes,

2. Dip the substrate in IPA for 30 seconds to stop developing.

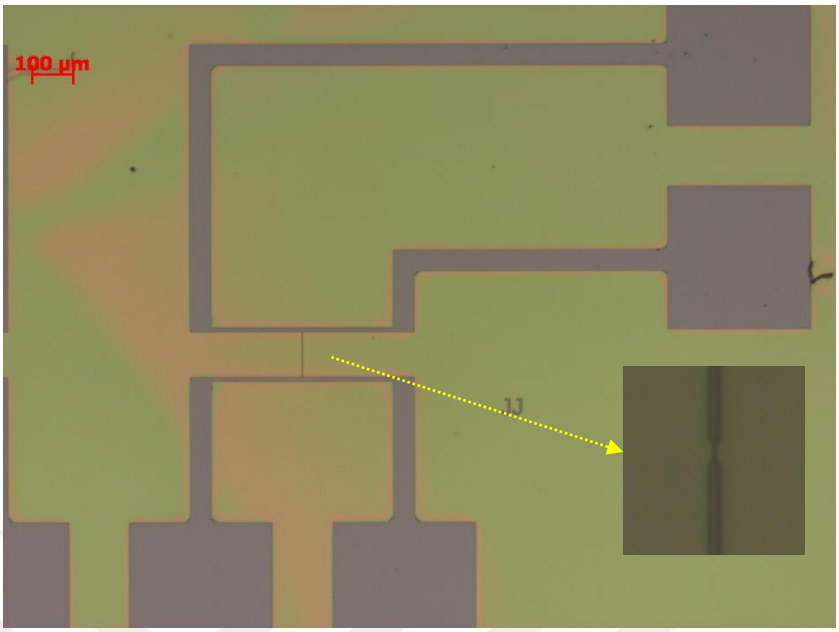


Figure 2.5: Microscope image of the substrate after developing process. Lighter green color shows the resist, darker gray colors show the areas that the resist is removed.

#### 2.1.3.6 Metal Deposition and Insulating Layer Formation

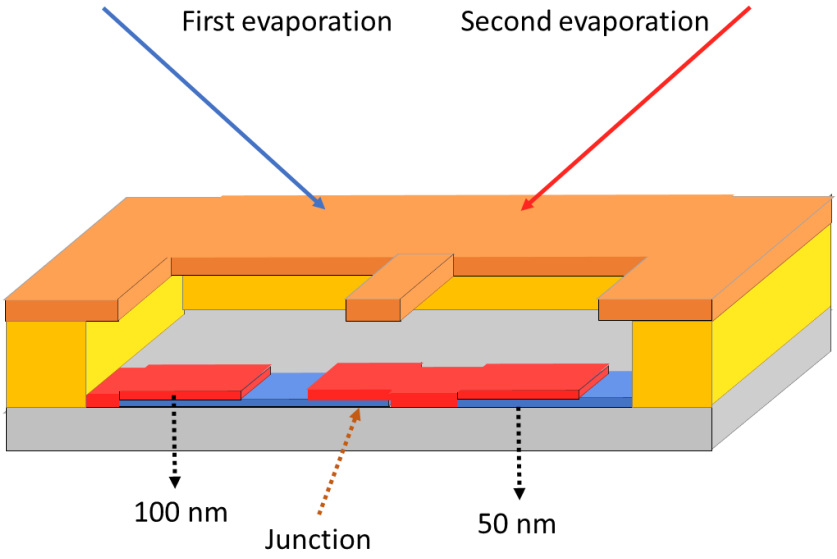


Figure 2.6: Illustration of shadow angle evaporation method.

Next step in the fabrication is to deposit aluminum layers and form the insulating layer in between. Various techniques have been used for fabrication of a metal-insulator-metal junctions. One of the most used one is called “shadow angle evaporation” or “Dolan bridge” [22]. To deposit aluminum, aluminum pellets are placed in a tungsten boat and evaporated by applying a controllable electrical current through the boat. This method is called “thermal evaporation.”

An illustration of shadow angle evaporation is shown in figure 2.6. First, the bottom layer (blue) of aluminum is deposited with an angle. The resist bridge creates a discontinuity in the deposited pattern. Then, the surface of the first layer of aluminum is oxidized in order to form the insulating layer. Finally, second layer of aluminum is deposited from the opposite side with the same angle (red layer), leading to formation of the junction.

For thermal evaporation, VAKSIS evaporation system located at SUNUM cleanroom is used. The geometry of the evaporation chamber shown in figure 2.7. Sample is loaded on the top side of the chamber, facing down. First layer is deposited from the crucible located at the left end. Then, the chamber filled with oxygen gas for oxidation. Finally, second layer is deposited from the crucible located at the right end.

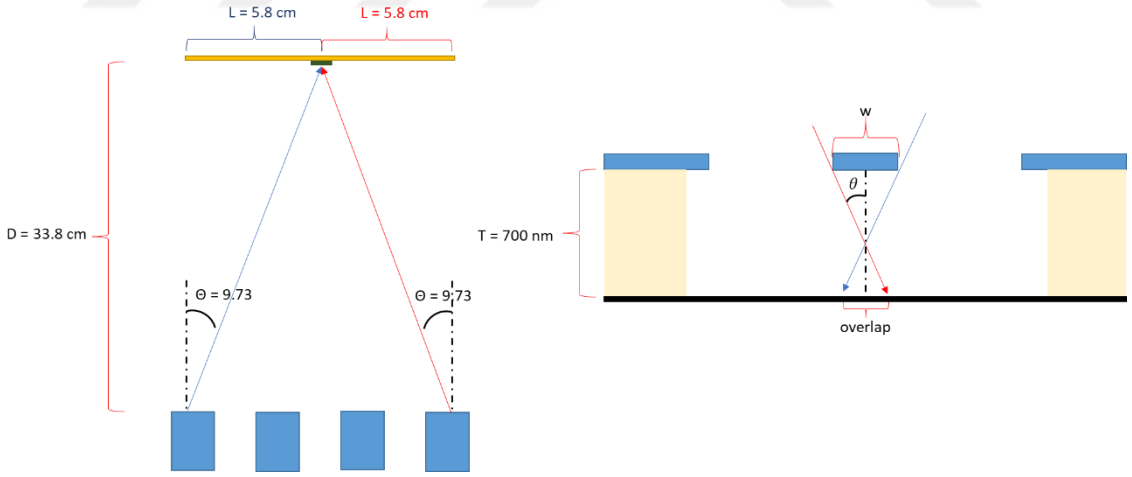


Figure 2.7: Configuration of the evaporation chamber (left) and geometry of shadow angle evaporation (right).

In figure 2.7, geometrical parameters of the method are shown. Using the geometry, the formula for junction overlap size is:

$$Overlap = 2T\tan(\theta) - W \quad (2\text{-}1)$$

Due to the configuration of the evaporation chamber, maximum possible evaporation angle was $\theta = 9.5^{o}$. I used a bridge width of W = 100 nm and the resist thickness was T = 700 nm. Using the above equation, expected junction length is about 130 nm; while its width would be the same as in the resist pattern as 200 nm.

While the thickness of the first layer of aluminum is 50 nm, the second layer is deposited thicker (100 nm) to prevent discontinued coverage at the edges.

The parameters of the deposition process as follows:

1. Pump down the chamber to base pressure (~2x10$^{-6}$ Torr),
2. Deposit 50 nm aluminum as the 1$^{st}$ layer under using the crucible at the left end,
3. Fill the chamber with oxygen gas until the pressure is 5 mbar,
4. Wait for 6 hours to ensure complete oxidation at room temperature,
5. Evacuate the chamber back to base pressure and deposit 100 nm aluminum as the 2$^{nd}$ layer using the crucible at the right end.

After metal deposition is finished, we need to remove the PMMA and the deposited metal on top of it. To do that, I dip the sample in acetone at 60$^{o}$ C for 10 minutes, or keep it in acetone for one day. This process called “lift off”, and we complete the fabrication of the circuit.

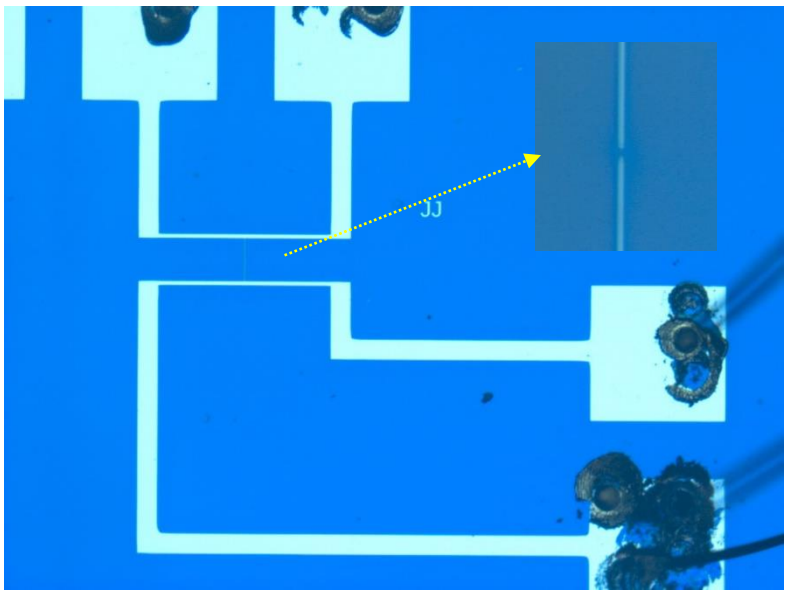


Figure 2.8: Microscope image of a sample after deposition.

#### 2.1.3.7 Mounting Sample in a Chip Carrier and Wirebonding

In order to connect the sample to the measurement instruments, the sample is mounted on a chip carrier and the contact pads of the sample are bonded to the pads of the chip carrier using a wire bonder. At SUNUM, we use TPT wire bonder for this purpose.

First, the substrate is fixed inside the chip carrier. To do that, a very small drop of PMMA inside the chip carrier is dropped and the substrate is put inside. After that, it is baked at 150 $^{o}$C for a few minutes so that the substrate sticks to the chip carrier.

The final step is wire bonding. Using the wire bonder. The pads of the sample are bonded to the pads of the chip carrier with gold wire. The final sample is shown in figure 2.9.

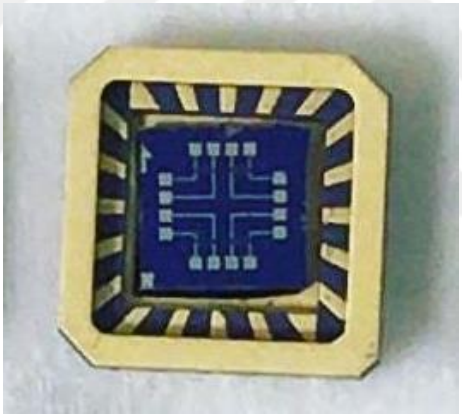

Figure 2.9: Sample mounted and wire bonded in a chip carrier, ready for measurement.

### 2.1.4 Fabrication of Alumina Deposited Josephson Junction

In this part, the fabrication process that is used for fabricating Al-$AlO_x$-Al Josephson junction with alumina deposition will be discussed in detail.

#### 2.1.4.1 Layout Design

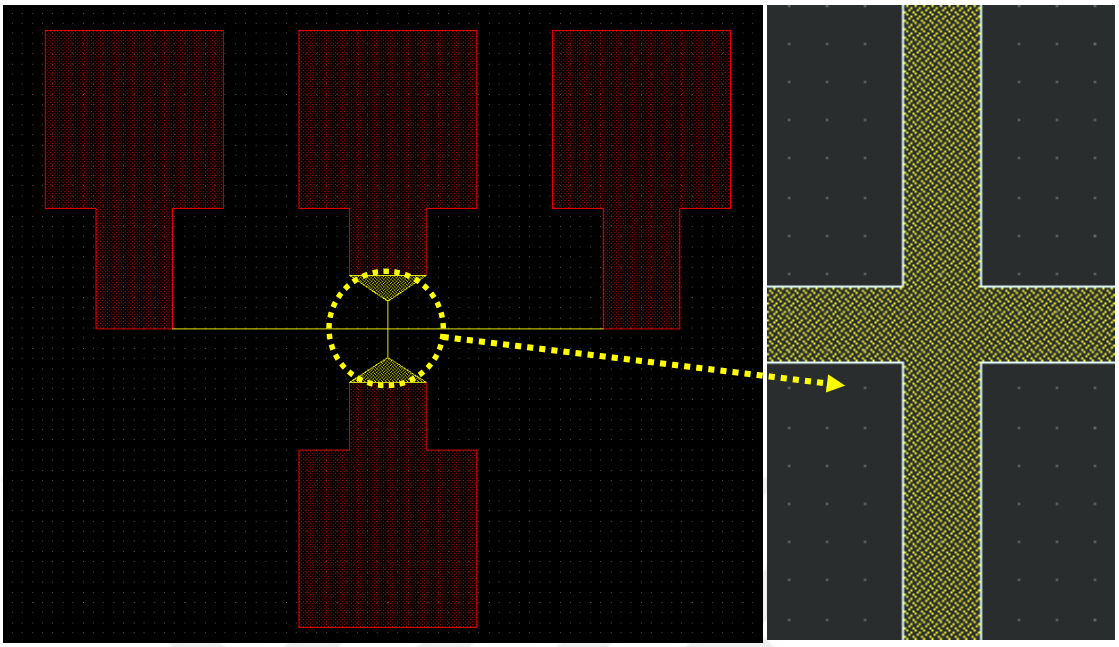

Figure 2.10: Layout design of the alumina deposited Josephson Junction.

Similar to the previous method, very thin patterns are separated to illuminate them with a better resolution value. This time, since a different metal deposition method is used, the design is different than before. A “+” pattern for the junction is designed. In order to implement the method correctly, each thin pattern of the junction has 100 nm width.

#### 2.1.4.2 Substrate Preparation

The exact same process is used as in section 2.1.3.2.

### 2.1.4.3 Coating PMMA on the Substrate

This time, a large undercut profile is not desired. Thus two layers of PMMA with only slightly different molecular weights are used; PMMA 495/C6 resist for the bottom layer is used whereas for the top layer PMMA 950/A4 is used. The coating process is as follows:

1. Spin coat the substrate with PMMA 495/C6 with spin speed 2500 rpm/min for 55 seconds,
2. Bake the substrate at 170 °C for 5 minutes,
3. Spin coat the substrate with PMMA 950/A4 with spin speed 2500 rpm/min for 55 seconds,
4. Bake the substrate at 170 °C for 5 minutes.

### 2.1.4.4 Patterning with EBL

Same process is used as before including proximity effect correction. However, this time 850 μC/cm$^2$ is used for the dose value.

### 2.1.4.5 Developing the Patterned Substrate

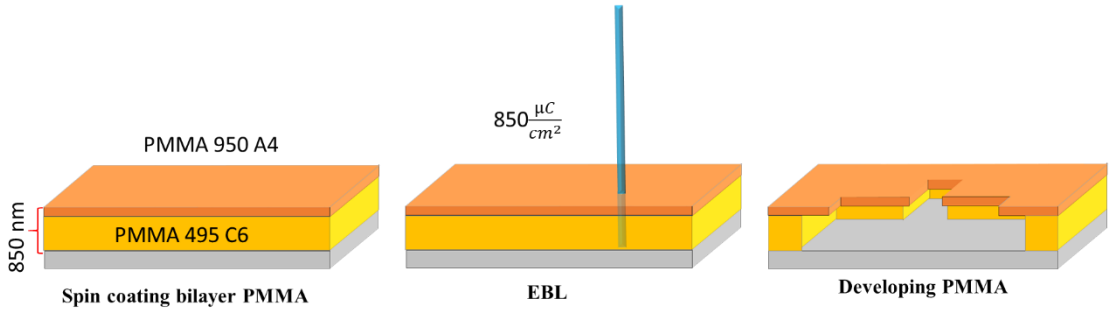


Figure 2.11: Illustration of development process. The substrate coated bilayer PMMA and patterned with EBL using the dose value shown in figure, finally developed and the pattern is formed for "+".

The same developer is used as the previous method. But the percentage and the process used are different. The development recipe as follows:

1. Dip the substrate in 1:3 MIBK:IPA for 1 minute,
2. Dip the substrate in 1:1 MIBK:IPA for 10 seconds immediately after the 1st step,
3. Dip the substrate in IPA for 30 seconds to stop developing.

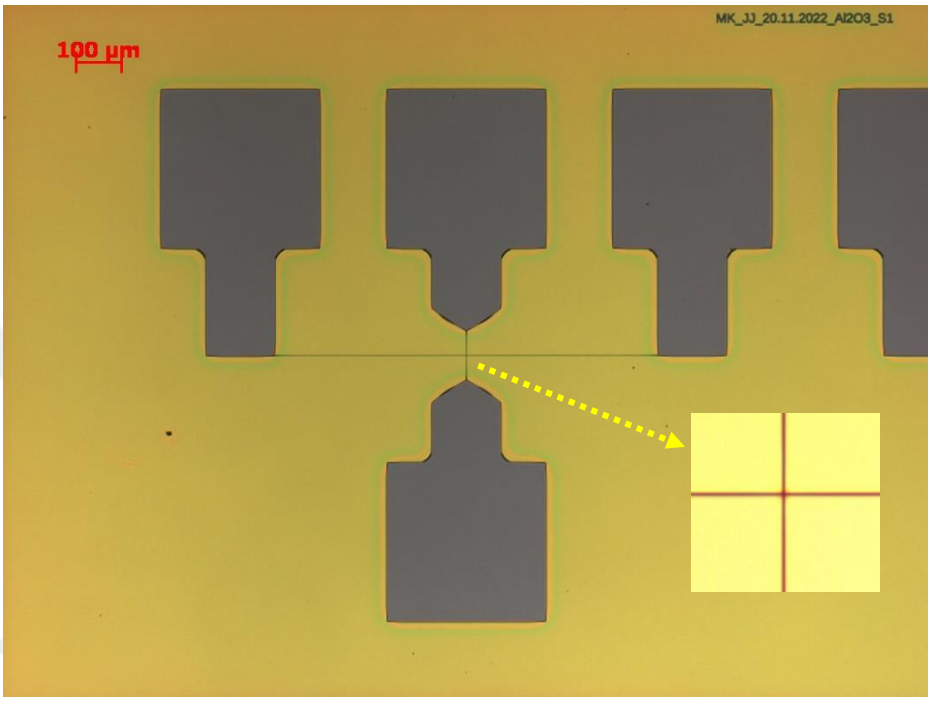


Figure 2.12: Microscope image of the sample after developing.

#### 2.1.4.6 Metal Deposition and Insulating Layer Formation

The goal is to deposit only one line at each deposition, on the line parallel to the deposition direction. The aim is to have no deposition on the line perpendicular to the deposition direction. I first deposit the 1st layer of aluminum to the horizontal line, then deposit alumina to the vertical line, finally deposit the 2nd layer of aluminum on the vertical line. This way a junction is formed at the cross section of the "+".

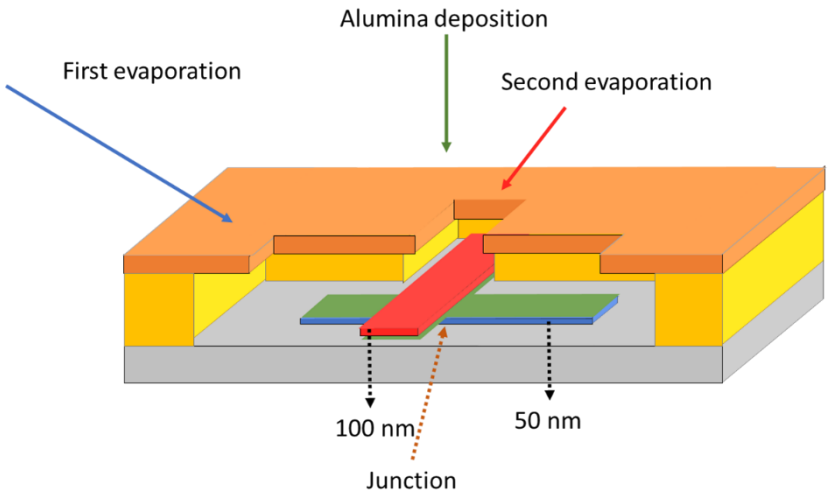


Figure 2.13: Illustration of "+" evaporation method.

The geometry of the TORR evaporator is shown in figure 2.14.a). The e-beam evaporator is in the middle and alumina can only be deposited using e-beam evaporation. Aluminum is deposited using the crucible located on the left. Therefore, we implemented the following process:

The parameters of the deposition process as follows:

1. Evacuate the camber to its base pressure (~$9x10^{-6}$ Torr)
2. Deposit 50 nm aluminum as the 1st layer of using the crucible at the left end,
3. Rotate the sample holder 90°,
4. Deposit 1.9 nm alumina as the insulating layer using the e-beam evaporator located at the center,
5. Deposit 100 nm aluminum as the 2nd layer using the same crucible.

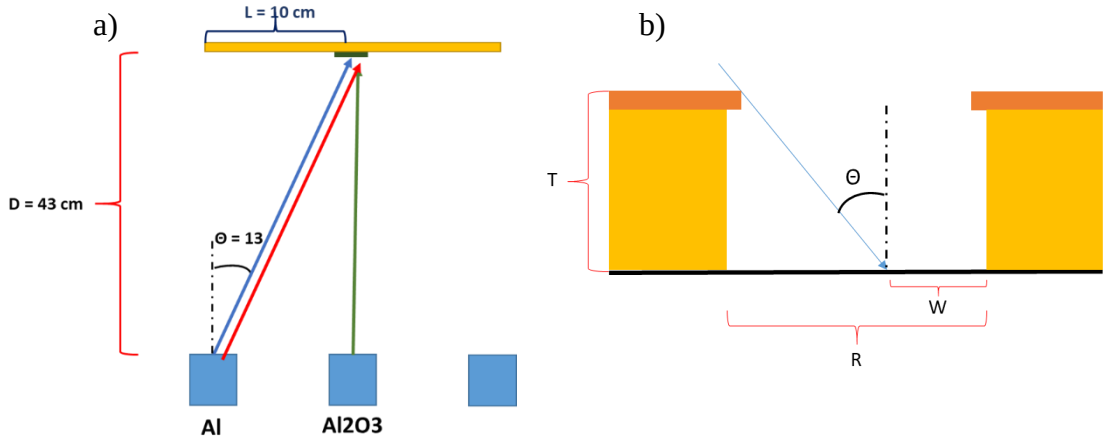


Figure 2.14: Evaporation chamber geometry and deposition parameters. a) TORR chamber configuration, sample should be rotated 90$^{o}$ after first deposition in order to implement the method. b) Geometry of deposition for the perpendicular line pattern to the evaporation direction. The goal is to deposit no metal to the perpendicular pattern,

In figure 2.14.b), geometrical parameters of the method are shown. Using the geometry, the formula for the width of the deposited metal is:

$$W = R - T\tan(\theta) \qquad (2\text{-}2)$$

Where $W$ is the width of the metal deposited, $R$ is the width of the developed area, $T$ is the resist thickness and $\theta$ is the evaporation angle. Due to the geometry of the evaporation chamber, maximum evaporation angle for aluminum is $\theta = 13^{o}$. The metal width "$W$" is needed to be zero, since the goal is to have no deposition on the line perpendicular to the evaporation direction. The resist thickness is 850 nm. Thus, using the formula, width of the line $R$ should be less than 100 nm.

Finally, the lift off process exactly the same as explained in section 2.1.3.6 is conducted.

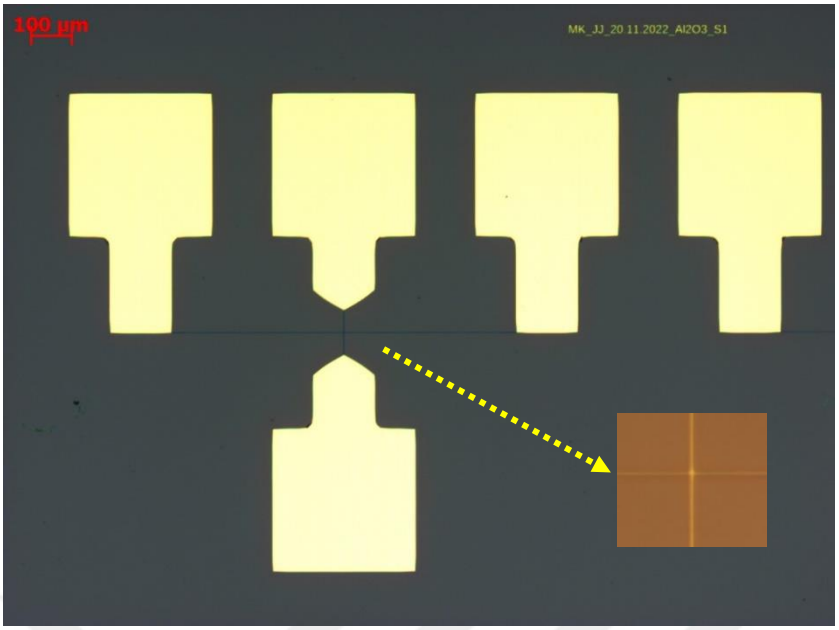


Figure 2.15: Microscope image of the sample after deposition.

#### 2.1.4.7 Mounting Sample in a Chip Carrier and Wirebonding

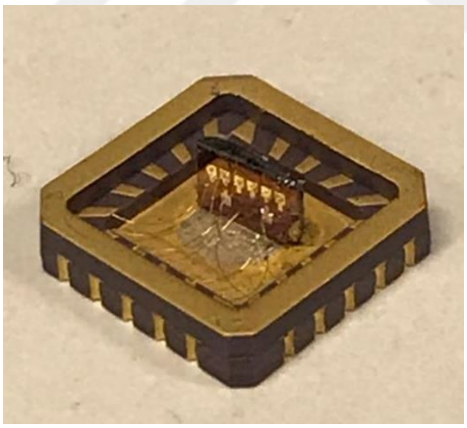

Figure 2.16: Sample mounted and wire bonded on a chip carrier. This time, sample is mounted perpendicularly.

The exact same method explained in section 2.1.3.7 is implemented. However, this time, in order to apply magnetic field parallel to the insulating layer, the substrate is mounted perpendicular as shown in figure 2.16.

## 2.2 Characterization of Josephson Junction

In this subsection, the measurement process is discussed. First, the measurement methods, then the measurement setup and the instruments are mentioned. Finally, the measurements conducted and their purposes are discussed.

### 2.2.1 Measurement Technique

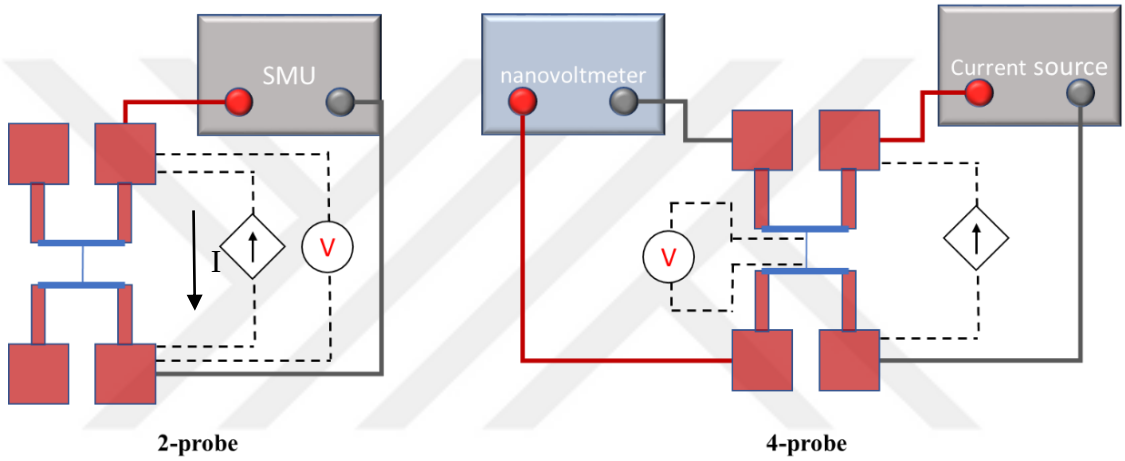


Figure 2.17: 2-probe and 4-probe I-V measurements. In 2-probe method, current/voltage application and measurement are conducted using the same leads with the same instrument. In 4-probe method, measurement is conducted using a separate instrument and a separate pair of leads.

In order to characterize the devices, an electrical measurement is needed to be conducted. For this purpose, 2-probe and 4-probe measurement methods are used.

In 2-probe measurement, a current is applied and voltage is measured, or vice versa. The source measurement unit (SMU) or power source (PS) can conduct 2-probe measurement by default. The downside of this method is that the voltage drop on the connection cables and leads cannot be excluded. In the 2-probe method, a SMU applies current (voltage) and measures the voltage (current) from the same pair of sockets that it is connected. Therefore, the voltage at the instrument end also includes the voltage drop on the leads

all the way to the sample leading to error in the measurement. In order to eliminate this error, 4 probe method is used.

In 4-probe method, a current is applied to the sample. Using a second instrument such as nanovoltmeter, voltage is measured via a different set of leads connected directly to the device. Thus, the voltage on the device is measured since no current flows through the leads that are used to measure voltage.

### 2.2.2 Measurement Setup

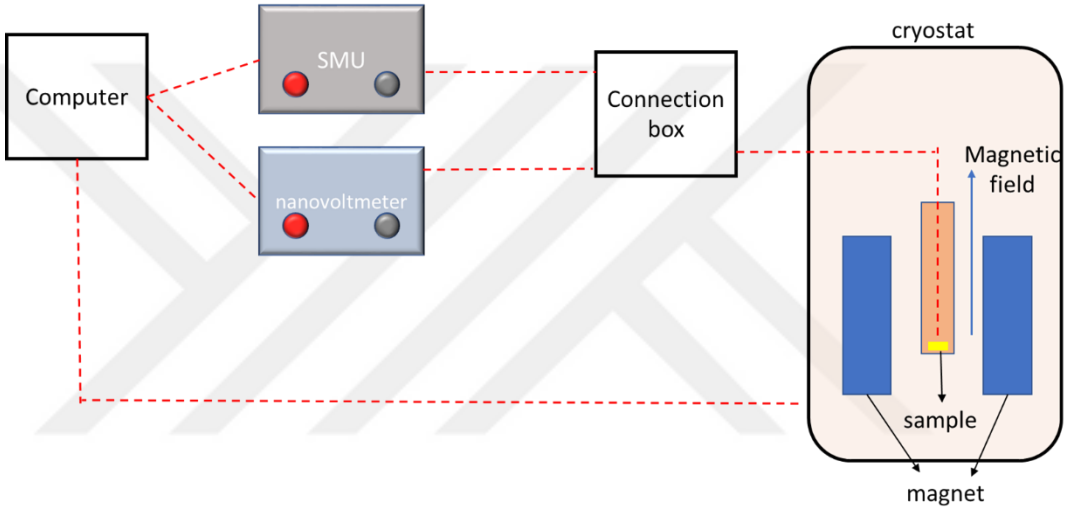


Figure 2.18: Measurement setup. The sample is loaded to the dilution refrigerator (cryostat). It is connected to measurement instruments through a connection box. A computer is used to conduct measurement and collect data.

To do the low temperature measurement, Triton 400 Dilution Refrigerator (DR) located at SUNUM is used. The DR has the base temperature of 10 mK and has a superconducting magnet that can apply a perpendicular magnetic field up to 12 T as shown in figure 2.18.

To measure the samples, we mount the chip carrier to the sample holder of the refrigerator and load the sample holder inside the chamber. When loaded, sample holder and thus the chip carrier is connected to the socket located outside of the refrigerator. Measurement instruments are connected to these sockets in order to be connected to the sample. For

electrical measurements, a source measure unit (SMU), a power source (PS) and a nano-voltmeter are used.

In order to follow certain measurement patterns and get the measurement data automatically, LabVIEW program is used. Using this program, we are able to control the instruments and the magnet of DR, sweep applied current, voltage or magnetic field values automatically. And the measurement data is automatically saved to a file.

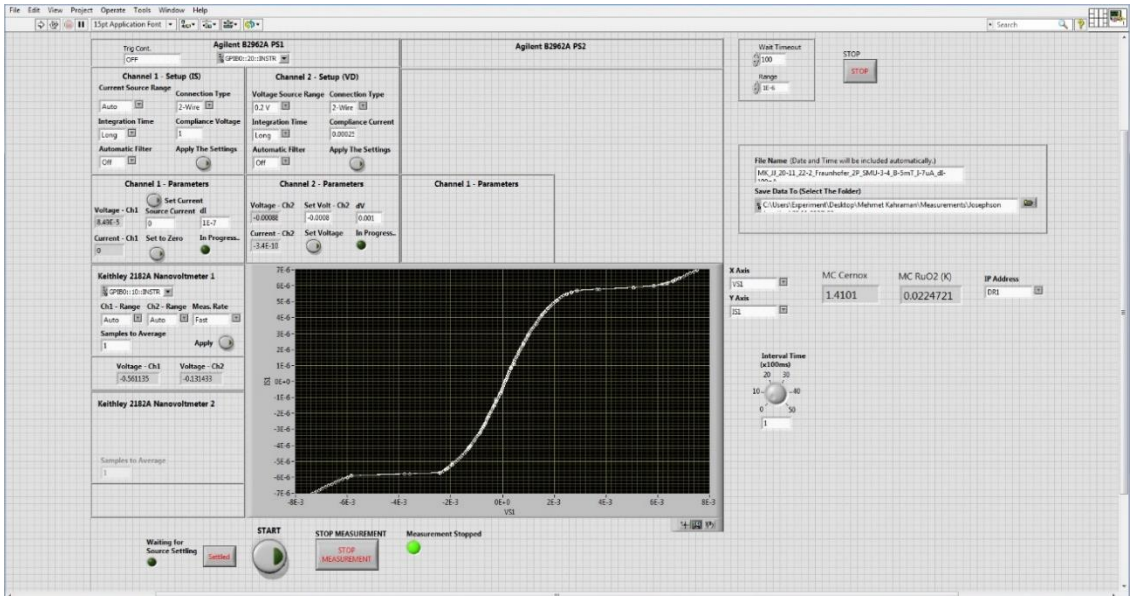


Figure 2.19: Screenshot of the LabVIEW program used for measurements.

### 2.2.3 Measurements Conducted on the Samples

First step is to check the contacts whether they are connected properly. To do that, 2-probe measurement is conducted between the short contacts. After confirming the contacts working properly, the measurements can be conducted on the sample.

In this thesis, mainly 3 type of measurements are conducted:

1. *Resistance-Temperature (RT) measurement*: In order to confirm the superconductivity of a sample, the behavior of samples under temperature change should be observed, especially under the critical temperature. To achieve this, RT measurements are conducted. A continuous steady current is applied to the sample

while the sample is cooling down, and the voltage is measured. Mainly 4-probe technique is used for this measurement, but 2-probe technique could be used as well if needed.

2. *I-V measurement*: The most important measurement is the I-V measurement of the junction. As discussed in chapter-1, I-V characteristics gives detailed information about the junction; whether it is overdamped or underdamped, what is the critical current and retrapping current if any, whether there is any hysteresis. To take the I-V measurement, we start from 0 A current and sweep through a positive current $I_{max}$, then sweep down to $-I_{max}$, finally sweep back to 0. Both 4-probe and 2-probe measurements are used for this purpose.
3. *$I_c$ vs Magnetic Field (Fraunhofer) measurement:* The purpose of this measurement is to check whether we observe a Fraunhofer pattern and if so what kind of pattern it is. To do this measurement, I-V measurement is conducted as magnetic field is varied in steps. Magnetic field is kept constant during an I-V measurement and then increased to the next step for the following measurement. The critical current $I_c$ for each magnetic field value is determined from I-V curves and the critical current vs magnetic field curve is plotted.

# 3. RESULTS AND DISCUSSION

In this section, results of the fabrication and measurements for each type will be presented.

## 3.1 Samples with Oxidized Insulating Layer

Two sets of samples are fabricated; named as SO1 and SO2. The only difference between SO1 and SO2 is the width of the top aluminum layer. The top layer of SO1 is 5 times wider than the bottom layer, whereas it is the same as the bottom layer for SO2.

SO1 consists of three devices; named as SO1_D1, SO1_D2 and SO1_D3. All devices are fabricated on the same 1 cm x 1 cm substrate and fabricated under the same conditions. SO1_D3 is used only to take SEM images, since SEM imaging may contaminate or damage an electronic device, one sample is dedicated for SEM imaging only. 2 of them are used for measurements. Due to the fact that the fabrication processes are exactly the same for all the devices, we can compare the results and determine the repeatability of the method. In addition, it can also be assumed the geometry of the devices are identical and the SEM images apply to all the samples in the same batch.

SO2 consists of four devices; named as SO2_D1, SO2_D2 and SO2_D3. Similarly, they are fabricated on the same substrate under the same condition. SO2_D3 is used for SEM imaging, whereas the others are measured.

### 3.1.1 Results of SO1

The SEM image of SO1_D3 is shown in figure 3.1. It is clear from the image that the junction formation is successful. The dimensions of the junction are approximately 130 nm x 200 nm, almost identical to the measured dimension.

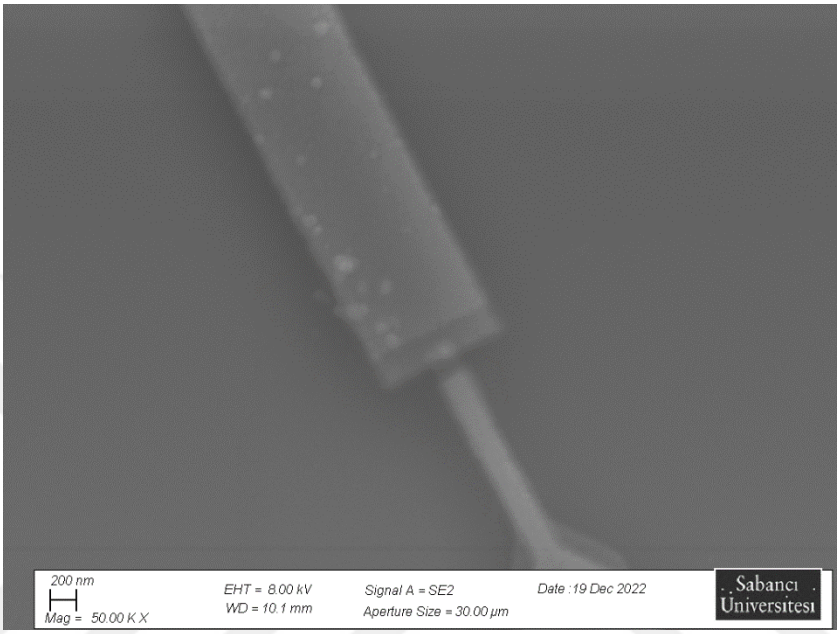


Figure 3.1: SEM image of SO1_D3 device that is fabricated with shadow angle evaporation method.

#### 3.1.1.1 R-T Graph

The R-T graph of SO1_D1 and SO1_D2 are shown in figure 3.2. When a metal switches to its superconducting state, we expect a sudden drop in the resistance to zero. Considering the results, the graph of SO1_D2 shows a sudden drop at around 0.93 K, indicating that they switch to the superconducting state at the critical temperature of aluminum (~1.2 K). Whereas, SO1_D1 not only doesn't switch to superconducting phase, but also its resistance increase as the temperature decrease, which is unexpected for metals. This pattern suggests a semiconductor behavior which we attribute to severe oxidation of aluminum during its evaporation.

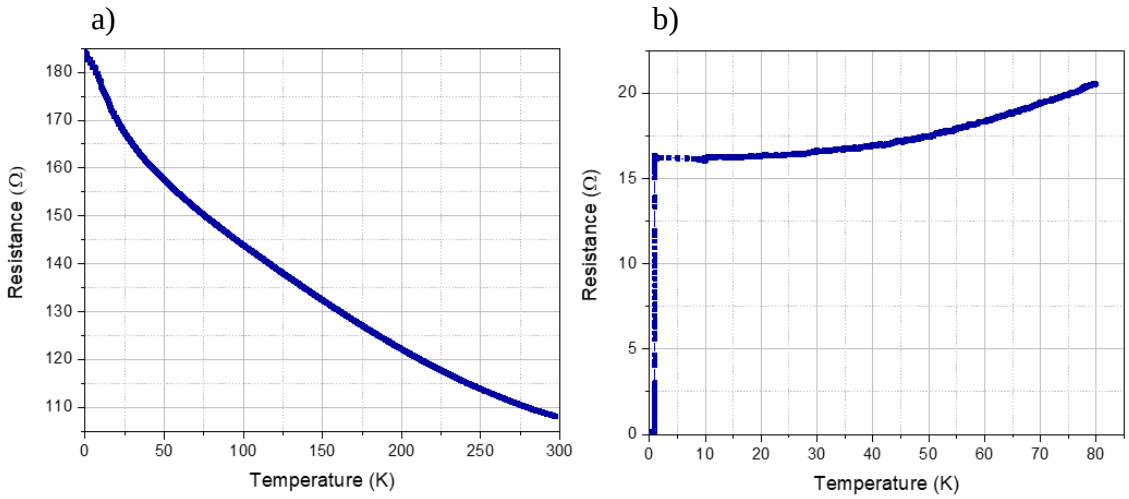


Figure 3.2: R-T curves of SO1_D1 and SO1_D2. a) SO1_D1 which shows characteristic R-T curve of a semiconductor, b) SO1_D2 which shows characteristic R-T curve of a superconductor.

### 3.1.1.2 I-V Characterization

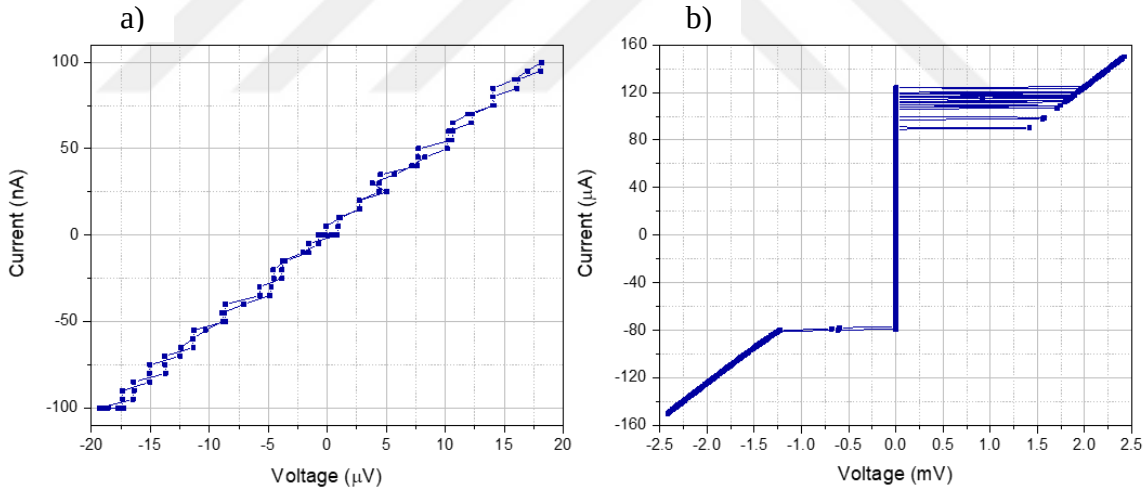


Figure 3.3: I-V curves of a) SO1_D1 which shows no junction behavior and b) SO1_D2 which shows the characteristics of an underdamped Josephson junction

The I-V measurement results of SO1_D1 and SO1_D2 are shown in figure 3.3. As expected, SO1_D1 does not show any junction I-V characteristics, but rather a linear curve. However, SO2_D2 results in the I-V curve of a junction.

In SO2_D2, critical current in the positive region is observed to be 124 μA, and the retrapping current is observed to be 106 μA; in the negative region they are observed as -79 μA and -77 μA respectively. Thus, both junctions are underdamped junctions. However, especially in the positive region there is a large hysteresis.

Since in the normal state $V = IR_n$; using the results from figure 3.3.b), for both negative and positive side, and using this formula it is calculated that $R_n \sim 16\,\Omega$. Inserting this value to equation 1-15, critical current is calculated as $I_c = 33\,\mu A$ which contradicts to the observed critical current value. If the observed critical current is assumed to be correct and $R_n$ is calculated using equation 1-15, it is found as $R_n \sim 4\,\Omega$. The difference in $R_n$ for the calculated values may be due to the resistance of thin superconductors at the junction area.

The differences in the hystereses can be caused by the width difference between bottom and top layers. The width of the top layer is 5 times wider and 2 times thicker than the bottom layer. When current is positive, electrons flow from the wider lead to the narrower lead and vice versa. More hysteresis in the positive region and less hysteresis in the negative region suggest that these hystereses may be caused by this dimension difference. It might be due to the fact that when sweeping through positive currents, the current is forced to flow from a wider lead to a much narrower one. Thus, the current is forced to confined to a much smaller volume. This might be causing the narrower lead to prematurely switch to normal state and might be causing a heating in the junction area, Moreover, heat conductivities of the superconductor are different since their dimensions different. Consequently, there might be temperature difference in the junction region causing such hysteresis. Further investigation is needed to confirm these hypotheses.

#### 3.1.1.3 Magnetic Field Characterization

Magnetic field-$I_c$ graph of SO1_D2 is shown in figure 3.4. In figure 3.4.a), theoretical Magnetic field-$I_c$ curve is plotted using equation 1-35 and using the observed values from the I-V characterization. The sample is mounted to the dilution refrigerator in a way that the applied magnetic field will be perpendicular to the sample. Measurement is conducted by taking I-V measurement under various magnetic field steps. Critical current value for

each sweep is determined by taking the highest current value for which the device is superconducting.

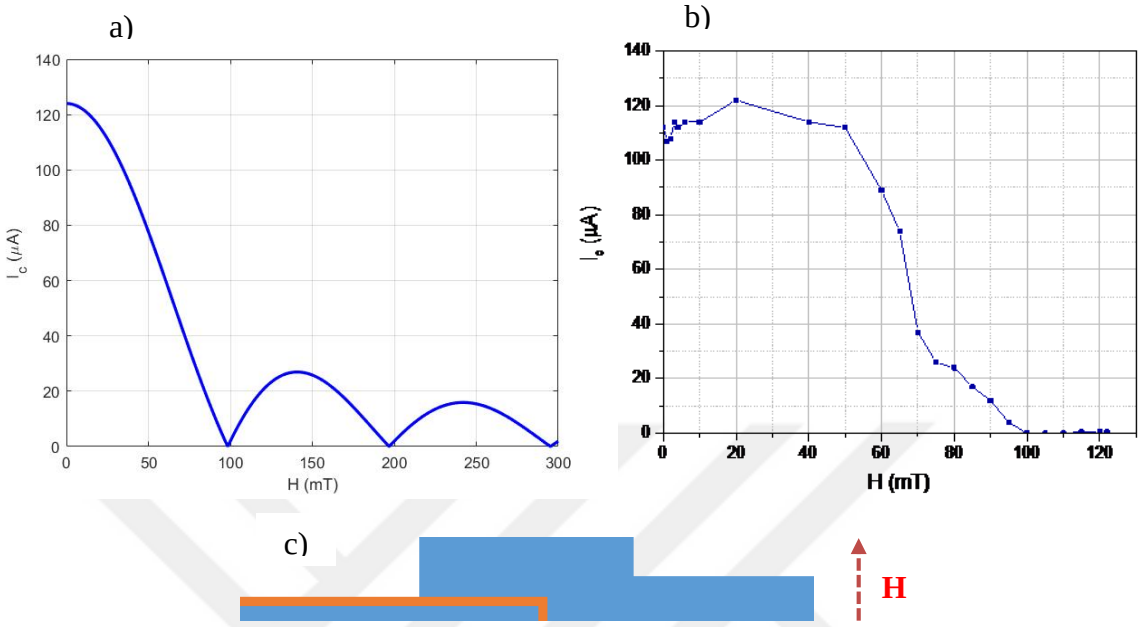


Figure 3.4: Magnetic field-critical current curve of SO1_D2. a) theoretical curve plotted using equation 1-35, for the actual device dimensions and material b) the measured $I_c$ vs H curve. c) the measurement configuration, thin orange line represents the insulating layer while the blue blocks represent superconductors. Only a very small portion of the insulating layer is parallel to the applied magnetic field.

A Fraunhofer pattern could not be observed in the magneto-transport measurement. This can be explained by the fact that since the magnetic field should have been parallel to the insulating layer, as shown in figure 1.9, and in the measurement configuration the much larger portion of the insulating layer is perpendicular, as shown in figure 3.4.c), the parallel side might be too small to observe a pattern.

From equation 1-35, using $\varphi_0 = HL[2\lambda_L + t]$, one can calculate the magnetic field value that the critical current will be zero for the first time. I calculated $H \sim 100\, mT$, which concurs with the experimental data.

### 3.1.2 Results of SO2

The SEM image of SO2_D3 is shown in figure 3.5. It is clear from the image that the junction formation is successful. The dimensions of the junction are approximately 150 nm x 200 nm, almost identical to the designed dimensions.

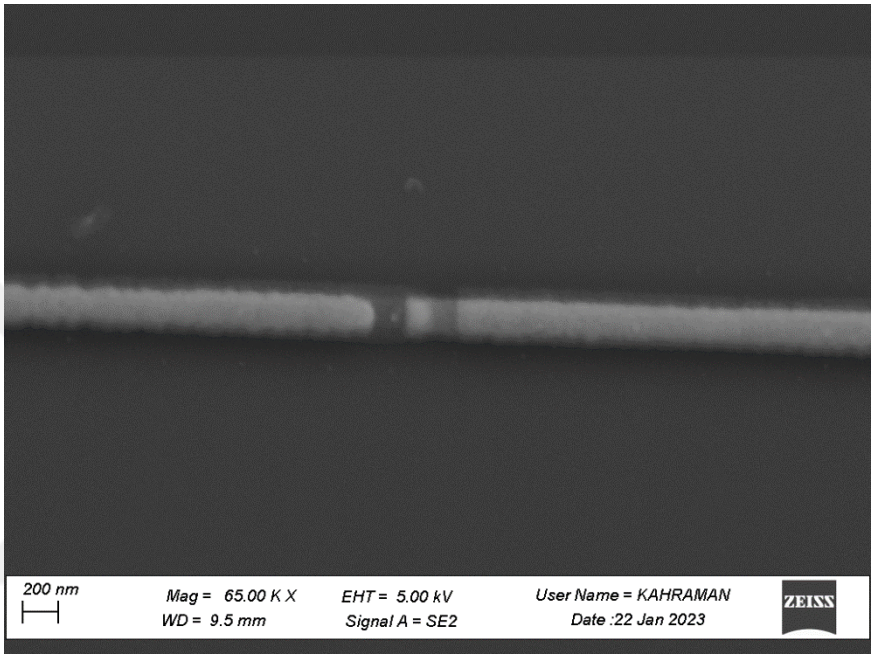


Figure 3.5: SEM image of SO2_D3 showing successful overlap of two aluminum layers.

#### 3.1.2.1 R-T Graph

R-T curve of sample SO2_D2 is shown in figure 3.6. At around 496 mK, the device switches to superconducting state, instead of literature value for the critical temperature ~1.1 K. This might have been caused by the applied current (3 μA) being too high. Nevertheless, the device is superconducting.

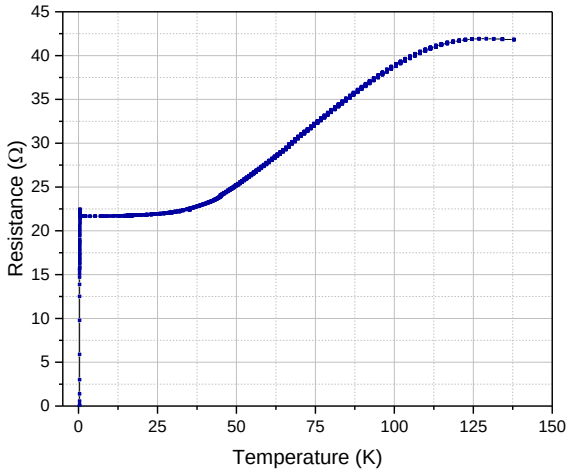


Figure 3.6: R-T curves of SO2_D2.

### 3.1.2.2 I-V Characterization

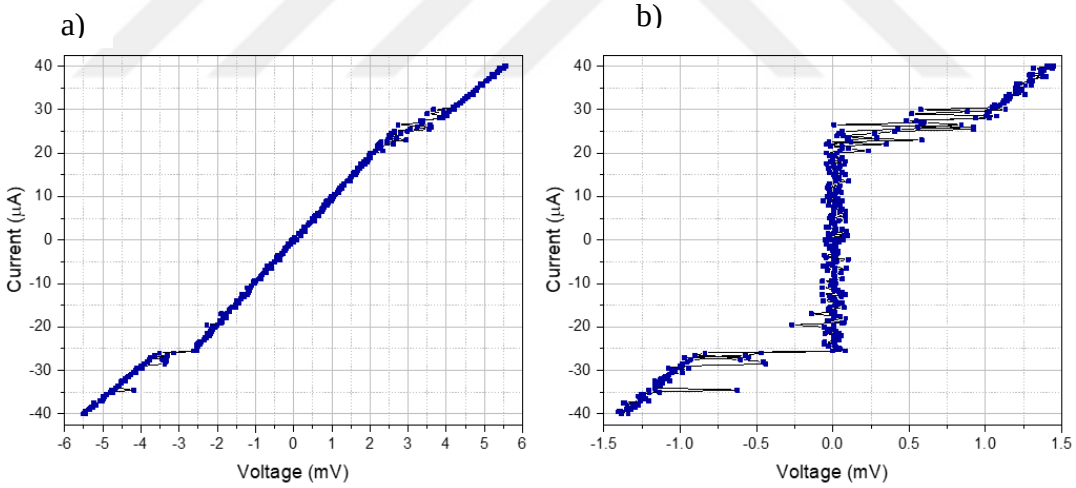


Figure 3.7: I-V curves of SO2_D1. a) I-V taken by a 2-Probe measurement, b) corrected I-V curve of the sample by subtracting the lead resistance from the results.

The I-V curves of SO2_D1 is shown in figure 3.7. One of the contacts of the sample were disconnected, thereby conducting a 4-Probe measurement was impossible. Instead, a 2-Probe measurement is conducted. By subtracting the lead resistance from the result a

clearer I-V characteristics is observed as shown in figure 3.7.b). It is clear from the figure that the device has a junction I-V characteristics.

By investigating figure 3.7.b), the critical current is estimated to be $I_c \sim 27\ \mu A$, and no retrapping current is observed. Assuming that the device is underdamped, and using $V = IR_n$ for the normal state and equation 1-15, the critical current is calculated as $I_c \sim 15\ \mu A$. Assuming that the junction is overdamped, since no retrapping current is observed, by using equation 1-24, the resistance is calculated as $R \sim 400\ \Omega$. Inserting this value into equation 1-15 will give $I_c \sim 1.5\ \mu A$. Considering the calculations and experimental results, it is assessed that this junction is not overdamped, rather underdamped.

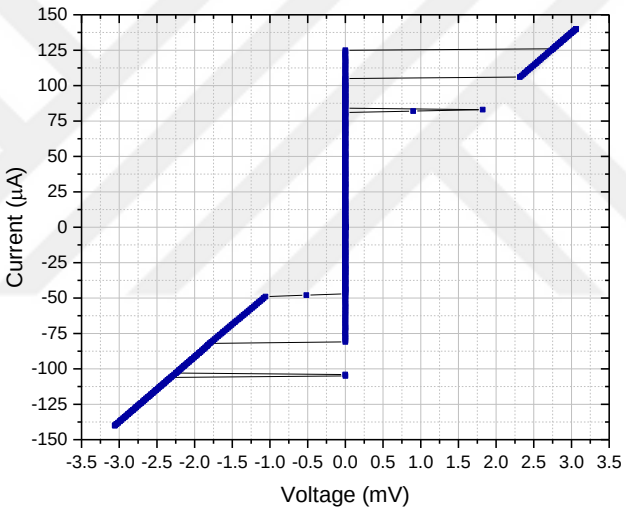


Figure 3.8: I-V characteristics of SO2_D2 which shows an underdamped Josephson junction behavior.

The I-V curve of SO2_D2 is shown in figure 3.8. It is clear from the figure that the device shows an underdamped junction behavior with extra hystereses. The critical and retrapping currents are clearer to observe. In the positive side, the critical current is observed to be 125 μA and the retrapping current is observed to be 105 μA. In the negative region, they are observed as -79 μA and -49 μA respectively.

Using $V = IR_n$, $R_n$ is calculated as $\sim 20\ \Omega$. Inserting this value into equation 1-15, the critical current is calculated as $I_c \sim 25\ \mu A$, which contradicts with the measured value. If the observed critical current is assumed to be correct and $R_n$ is calculated using equation

1-15, it is found as $R_n \sim 4\,\Omega$, similar to sample SO1_D2. Similar to SO1_D2, the difference in $R_n$ might be due to the resistance of thin superconductors at the junction area.

Aside from the critical and retrapping currents, premature switching to superconducting state is observed in both negative and positive sides of the curve. Hysteresis in the positive region is only observed while sweeping through positive side, not while sweeping back to zero current. In addition, hysteresis in the negative region is observed only when sweeping the current back to zero current. The hysteresis might be caused by thermal fluctuations. Due to the measurement configuration, while sweeping current in through the positive region the current flows from the top layer of aluminum through the bottom one, and vice versa. Since the top layer of aluminum of the device is twice thicker than the bottom layer, the bottom layer lead might be switching to normal state prematurely, thereby getting heated and heating the junction area. This might result in the premature switching of the device to the normal state, On the contrary, while sweeping back in the negative region, top layer switches to superconducting state prematurely due to its size, cooling the junction area for a short time, resulting in switching to superconducting state.

#### 3.1.2.3 Magnetic Field Characterization

Magnetic field-$I_c$ graph of SO2_D2 is shown in figure 3.9. Theoretical Magnetic field-$I_c$ curve is plotted using equation 1-35 and using the observed values from the I-V characterization. The device is mounted to the chip carrier vertically, so that when loaded to the dilution refrigerator, the substrate surface and hence the insulating layer will be parallel to the applied magnetic field. However, a Fraunhofer pattern could not be observed in the measurements.

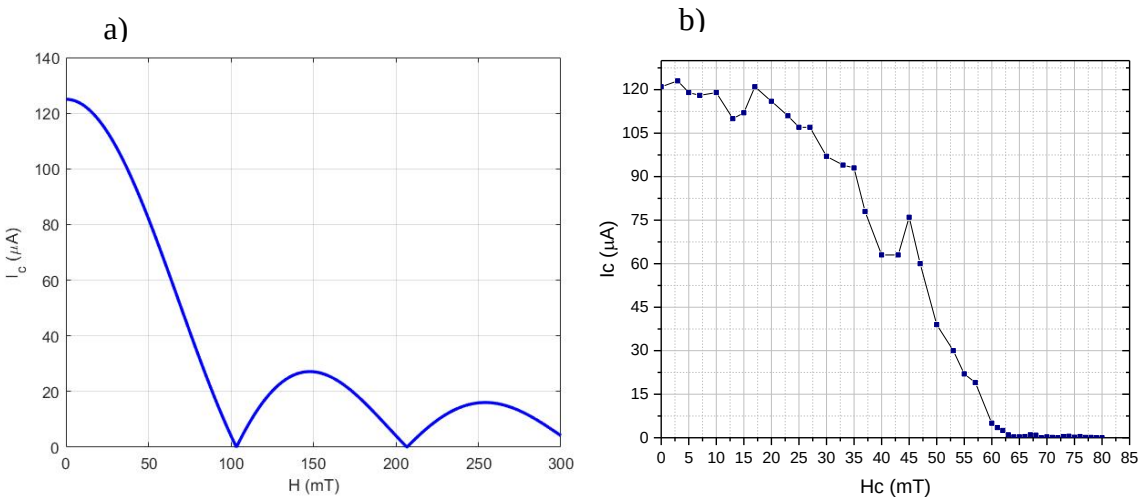


Figure 3.9: Magnetic field-critical current curve of SO2_D2. a) theoretical curve plotted using equation 1-35, b) experimental results. On the contrary to SO1_D2, the insulating layer is perpendicular to the applied magnetic field.

From equation 1-35, using $\varphi_0 = HL[2\lambda_L + t]$, one can calculate the magnetic field value that the critical current will be zero for the first time. I calculated $H{\sim}100\ mT$, which contradicts with the experimental data. The critical current becomes zero about $H{\sim}60\ mT$. This might be the reason that no Fraunhofer pattern is observed, although it is unclear what the reason is for the critical current becoming zero first time at a lower magnetic field.

### 3.1.3 Discussion on the Results of SO1 and SO2

For SO1, although we have successfully fabricated Josephson junctions, SO1_D2 is hysteretic and the other sample fabricated under identical conditions did not even become superconductive. This suggest that the fabrication method needs improvement. The hysteretic behavior of SO1_D2 near critical current is not observed on SO2_D2. This may suggest that the hysteresis was due to the size difference of the aluminum layers since SO2 has both layers with identical width. The reason for SO1_D1 not being superconducting can be explained by oxygen doping. Although the evaporation chamber was under high vacuum, there is residual oxygen gas inside the chamber which the aluminum atoms might react with during the deposition. In order to avoid this, a higher

deposition rate should be used. For SO1, the deposition rate was around 3 Å/s. A higher deposition rate or a better vacuum should be used while depositing aluminum.

Magnetic field measurement for SO1_D2 did not reveal a Fraunhofer pattern. As explained in the relevant subsection, this might be due to the large portion of the insulating layer being perpendicular to the magnetic field. The reason for this is the configuration of DR. Sample loader inside the DR is positioned in such a way that the chip carrier is perpendicular to the magnetic field. To overcome this issue, we tried to *mount the substrates perpendicular to the chip carrier* thereby positioning the insulating layer parallel to the magnetic in the following experiments.

For SO2, both samples showed Josephson junction behavior. In order to avoid doping, 10 Å/s deposition rate is used for SO2 fabrication which gave a successful result in achieving superconductivity in all devices. This suggests that the assumption of oxygen doping prevented the aluminum from becoming superconducting is valid. In addition, to examine whether the hysteresis observed in SO1_D2 is due to the size difference, SO2 fabricated with the same width of both layers of aluminum. Since any similar hysteresis is observed in both SO2_D1 and SO2_D2, this also suggest that the previous assumption on the effect of size is valid.

Similar to SO1_D2, magnetic field measurement for SO2_D2 did not reveal a Fraunhofer pattern. As explained in the relevant subsection, this might be due to the critical current becoming zero at a magnetic field value smaller than the expected value.

In both samples, the observed critical current and $R_n$ values contradict to the theoretical calculations. This might be caused by the narrow superconducting leads forming the junction being too long. The resistance of these leads cannot be avoided while conducting 4-Probe measurements.

## 3.2 Samples with Alumina Deposited Insulating Layer

Two sets of sample are fabricated; named as SA1 and SA2. The main difference between these samples is the PMMA recipe. SA2 is fabricated with the recipe presented in section 2.1.4.3. SA1 is fabricated with a different recipe, which resulted in 500 nm resist

thickness. As shown in the next section, the recipe is changed since the junction formation of SA1 was unsuccessful.

SA1 consists of three devices that are fabricated on the same substrate; named as SA1_D1, SA1_D2 and SA1_D3. SA1_D3 is used for SEM imaging while the others are measured. Similarly, SA2 consists of two devices, SA2_D1 and SA2_D2. SA2_D2 is used for SEM imaging while the other is measured.

### 3.2.1 Results of SA1

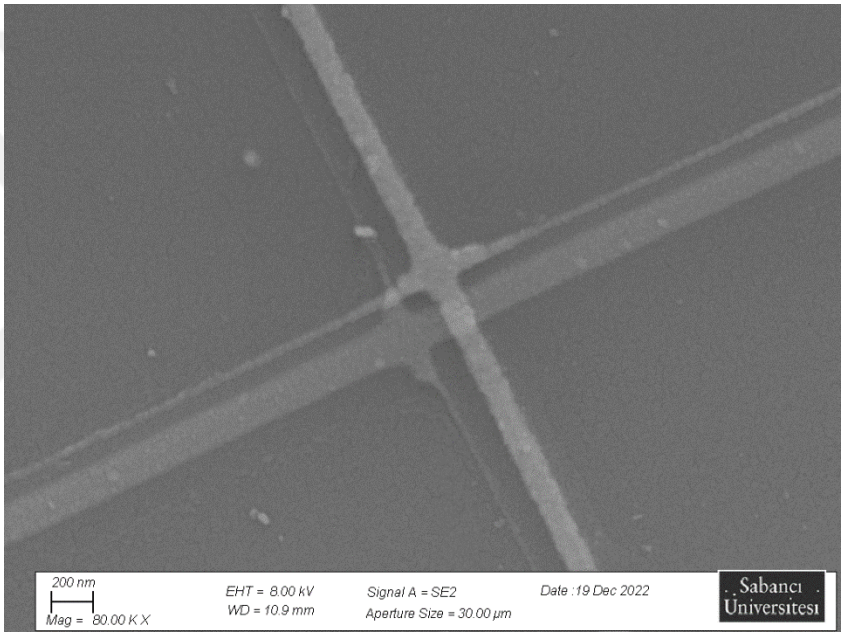


Figure 3.10: SEM image of SA1_D2 with alumina deposition. Wide lines are intended narrow lines are due to production failure. Conductance of the narrow lines speculative making it difficult to draw any conclusions from the electrical measurements.

The SEM image of SA1_D3 is shown in figure 3.10. It can be seen from the SEM image that the fabrication has failed to produce a single junction. When depositing layers, no aluminum was meant to be deposited on the patterns horizontal to the deposition direction. However, very thin lines of about 10 nm is deposited at both deposition steps. This resulted in a second small junction. Although the device geometrically resembles a SQUID, since the unintended junction is much smaller as well as the loop, it is difficult to do any clearly meaningful characterization.

### 3.2.1.1 R-T characterization

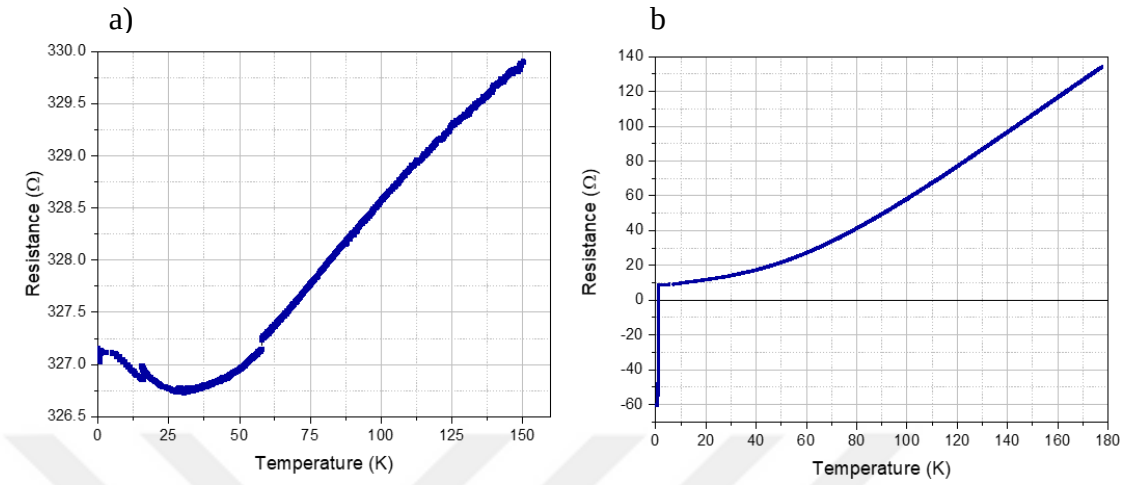


Figure 3.11: R-T curves of a) SA1_D1 shows no superconductivity, b) SA2_D2 which shows characteristic R-T curve of a superconductor, but also shows a negative resistance after certain point.

R-T graphs with 4-probe measurement of SA1_D1 and SA1_D2 are shown in figure 3.11. It is clear from the graph that SA1_D1 does not undergo a superconducting transition. On the other hand, Sample-2 shows a sudden drop in resistance below the critical temperature of 1.2 K. However, the resistance the 4-probe resistance becomes negative below Tc.

To verify the superconductivity, a 2-probe I-V measurement is also conducted on the contact leads excluding the junction. The results are shown in figure 3.12. As expected, we observe a sudden drop in the resistance down to 300 Ω, which is very close to the estimated total lead resistance. Thus, it is confirmed that SA1_D2 becomes superconductive.

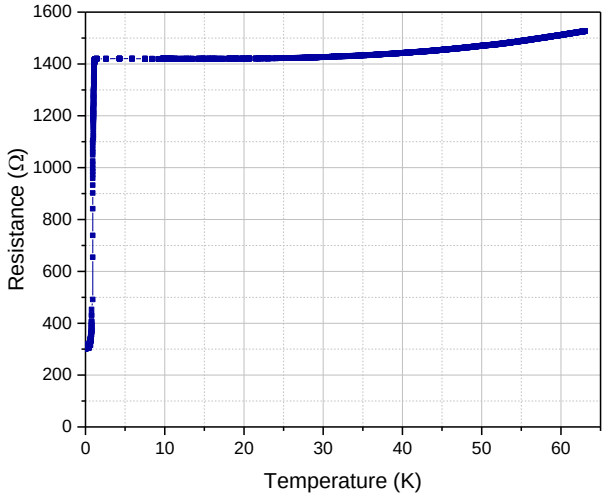


Figure 3.12: 2-probe R-T curve of SA1_D2.

### 3.2.1.2 I-V Characterization

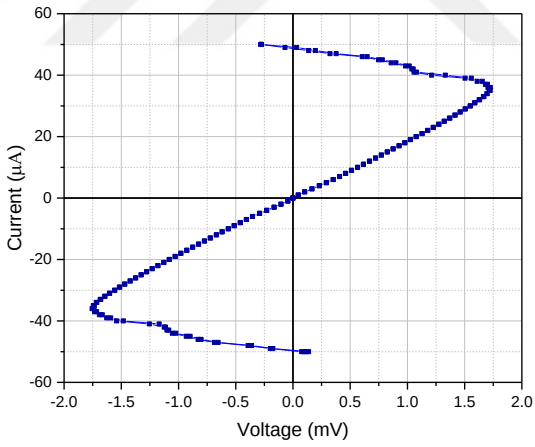


Figure 3.13: 4-probe I-V curve of SA1_D2.

I-V curve of SA1_D2 with 4-probe measurement is shown in figure 3.13. No junction behavior is observed from the 4-probe measurement results. In addition, an unexpected decrease in the voltage after 50 μA is observed. This can be because of the design. Using

4-probe measurement, we might actually have measured only the insulating layer; superconductors might only be behaving like the measurement probes.

In order to confirm the junction behavior, 2-probe measurement is conducted on the junction. The results are shown in figure 3.14. At 5.7 μA, a sharp increase is observed, suggesting that this value is the critical current value. In addition, no hysteresis and no retrapping current is observed. Moreover, the pattern is similar to an overdamped junction. Thus, the result resembles an overdamped junction.

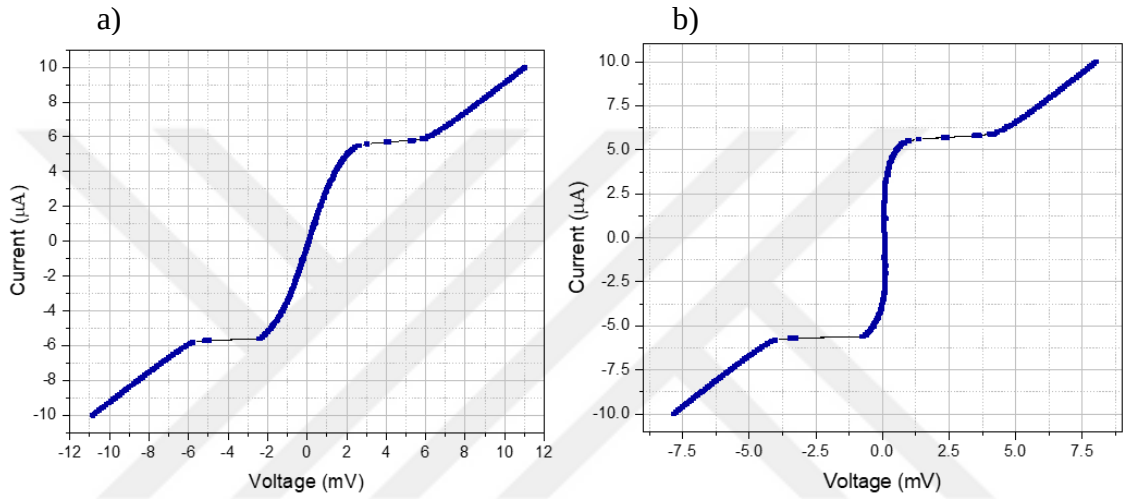


Figure 3.14: 2-probe I-V graph of SA1_D2. a) measured I-V curve, there is a sharp jump at 6 μA. The resistance in the superconducting region is contact resistance. b) the I-V curve in which the contact resistance subtracted from the data.

Using equation 1-35, and assuming the observed critical current value is valid, the resistance can be calculated as 1 kΩ. Using equation 1-15, $R_n$ can be calculated as approximately 100 kΩ. This difference might have been caused by the very long and narrow leads that form the junction which has length of 850 μm, causing a high resistance in the normal state.

### 3.2.1.3 Magnetic Field Characterization

Magnetic field- $I_c$ curve of SA1_D2 is shown. No Fraunhofer pattern is observed, although much larger portion of the insulating layer was parallel to the magnetic field. In addition, an interference is observed in the critical current values all the way down to zero critical current. The periodic behavior of the curve is similar to the behavior of a SQUID under a magnetic field.

From equation 1-35, using $\varphi_0 = HL[2\lambda_L + t]$, the magnetic field value that the critical current will be zero is calculated as $H{\sim}200\,mT$ for the junction dimensions that is intended to be fabricated. However, experimental data suggest that this value is $H{\sim}77\,mT$ which contradicts with the calculated value. This may suggest that the magnetic field pattern for a junction does not apply to this sample.

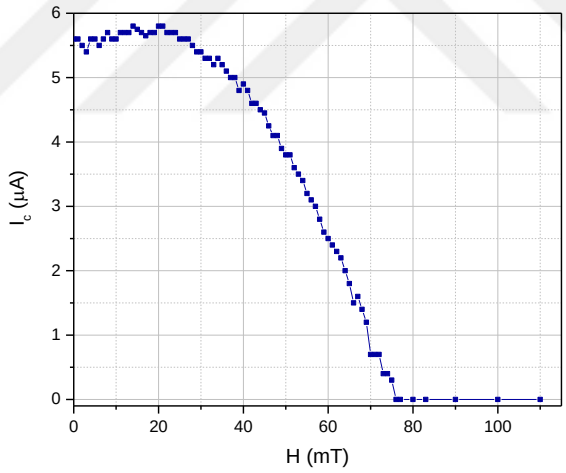


Figure 3.15: Magnetic field-critical current curve of SA1_D2. a) H-$I_c$ curve, b) I-V curve under various magnetic field values.

### 3.2.2 Results of SA2

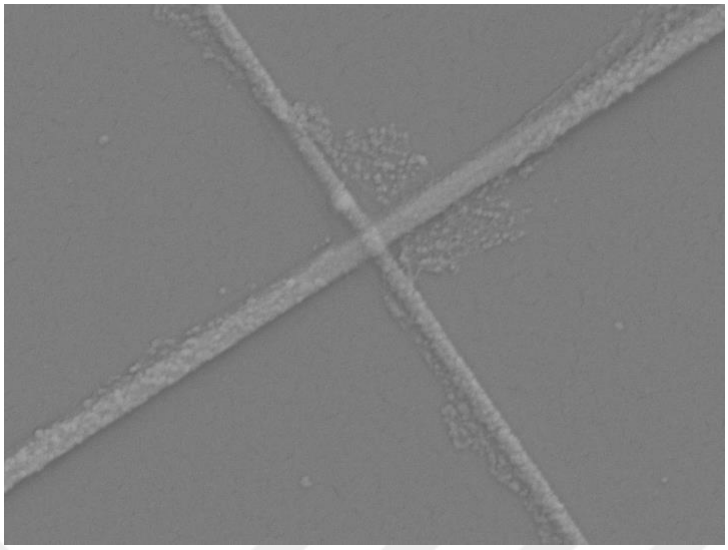

Figure 3.16: SEM image of SA2_D2 showing successful junction formation.

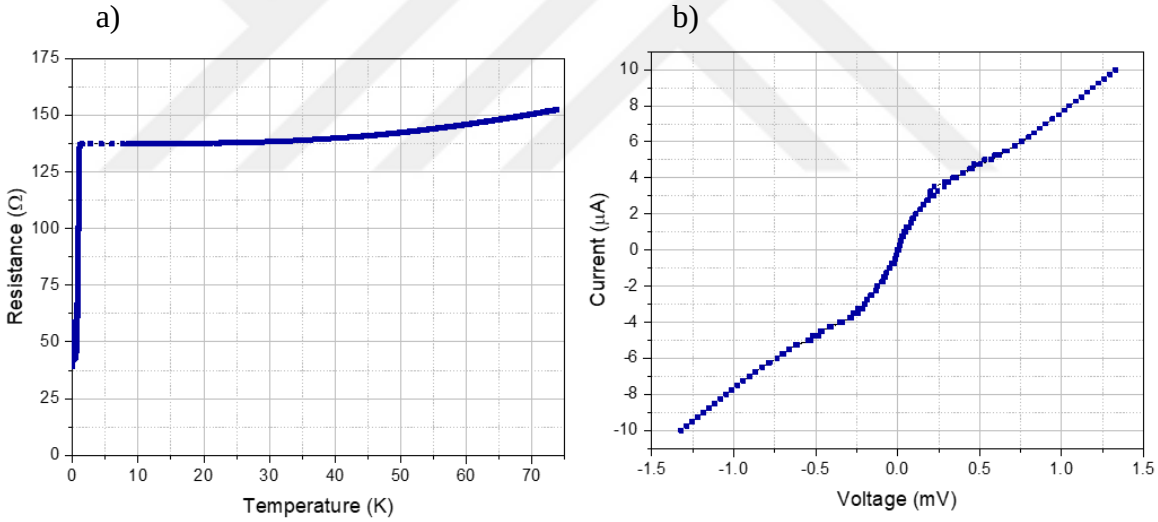


Figure 3.17: Characterization of SA2_D2, a) R-T curve shoving that the junction is not superconducting, b) I-V curve obtained by 4-Probe measurement.

The SEM image of SA2_D2 is shown in figure 3.16. The junction is successfully formed, as the PMMA recipe is updated due to the failure of SA1. R-T and I-V characteristics of SA2_D1 is shown in figure 3.17. It is clear from the figure that the device is not superconducting. It is assessed that the reason for this is the doping. Deposition rate of 1

Å/s is used during the fabrication. This might have caused aluminum to pick residual oxygen atoms inside the evaporation chamber, since the deposition rate is too small. No magnetic field characterization is conducted since the device is not superconducting.

### 3.2.3 Discussion on the Results

SA1 devices do not have a single junction geometry. This is caused by the fabrication process. The thickness of the resist was not high enough to prevent deposition of the unintended thin lines.

Due to the complexity of the sample, it is very difficult to characterize. However, the I-V curve indicates a junction behavior, which suggests that alumina deposition can be implemented for the insulating layer formation in junction fabrication.

Considering the interference and the magnetic field calculation in the previous section, a SQUID behavior under the magnetic field might have been observed. However, the pattern is not definite and may be due to measurement errors.

By updating the PMMA recipe, the junction formation successfully achieved in SA2 devices. However, the sample is not superconducting, since aluminum deposition rate is too small. A higher rate of aluminum deposition should be used as done in SO2 fabrication in order to achieve superconductivity in all devices.

# 4. CONCLUSION AND FUTURE WORK

In this thesis, we observed Josephson junction behavior in samples fabricated by using two different methods. However, for each of the methods there is still room for improvement for development of a repeatable fabrication method. For oxidized junctions, oxidation should be improved and further studied. In addition, better vacuum should be achieved before depositions in order to minimize the possibility of contamination, which may result in impurities or doping; we verified need for a high deposition rate for better material properties in evaporated aluminum. Furthermore, the length of the leads forming the junction should be minimized in order to prevent the effects of the lead resistance in the characterization of the junction.

In alumina deposited junctions, although a single junction geometry was not achieved, a Josephson junction behavior is observed. This suggest that alumina deposition can be used for insulating layer formation.

As the future work, it is assessed that alumina deposited junctions should be studied further, especially the effects of the insulating layer thickness on the quality of a junction. The effect of thickness should be studied by fabricating a number of junctions with varying insulating layer thicknesses.

The process for alumina deposited junction should also be improved. Especially the rotation of the sample during deposition can be improved by implementing electronic devices and controllers.

Another option can be using sputtering to deposit materials for junction fabrication. Certain sputter instruments have the configuration for implementing shadow angle evaporation.

## BIBLIOGRAPHY


[1] W. Anacker, “Josephson tunneling devices — A new technology with potential for high-performance computers,” *AFIPS Conf. Proc. - 1972 Fall Jt. Comput. Conf. AFIPS 1972*, pp. 1269–1278, 1972.

[2] J. M. Martinis, “Course 13 Superconducting qubits and the physics of Josephson junctions,” *Les Houches Summer Sch. Proc.*, vol. 79, no. C, pp. 487–520, 2004, doi: 10.1016/S0924-8099(03)80037-9.

[3] R. Combescot, *Roland Combescot*. 2005.

[4] R. Allls, B. Thermodynamics, and S. Mechanics Becker, “INTERNATIONAL SERIES IN PURE AND APPLIED PHYSICS Introduction to General.”

[5] P. H. E. Meijer, “Kamerlingh Onnes and the discovery of superconductivity,” *Am. J. Phys.*, vol. 62, no. 12, pp. 1105–1108, Dec. 1994, doi: 10.1119/1.17669.

[6] O. Kamerlingh, “Communications - Leiden 120b,” *Proceeding K. Akad. van Wet. Te Amsterdam*, vol. 120b, pp. 1479–1481, 1911.

[7] W. Meissner and R. Ochsenfeld, “Ein neuer Effekt bei Eintritt der Supraleitfähigkeit,” *Naturwissenschaften*, vol. 21, no. 44, pp. 787–788, 1933, doi: 10.1007/BF01504252.

[8] “Barone A & G Paterno, Physics and applications of Josephson effect (Wiley, 1982).pdf.”

[9] J. Bardeen, L. N. Cooper, and J. R. Schrieffer, “Theory of Superconductivity,” *Phys. Rev.*, vol. 108, no. 5, pp. 1175–1204, Dec. 1957, doi: 10.1103/PhysRev.108.1175.

[10] K. K. Likharev, “Superconducting weak links,” *Rev. Mod. Phys.*, vol. 51, no. 1,

pp. 101–159, Jan. 1979, doi: 10.1103/RevModPhys.51.101.

[11] “PL_1_251_1962_B_Josephson.pdf.”

[12] V. Ambegaokar and A. Baratoff, “Tunneling Between Superconductors,” *Phys. Rev. Lett.*, vol. 10, no. 11, pp. 486–489, Jun. 1963, doi: 10.1103/PhysRevLett.10.486.

[13] J. C. Woolley, *Introduction to solid state physics*, vol. 6, no. 1. 1957. doi: 10.1016/0022-5096(57)90051-0.

[14] W. C. Stewart, “CURRENT-VOLTAGE CHARACTERISTICS OF JOSEPHSON JUNCTIONS,” *Appl. Phys. Lett.*, vol. 12, no. 8, pp. 277–280, Apr. 1968, doi: 10.1063/1.1651991.

[15] D. E. McCumber, “Effect of ac Impedance on dc Voltage-Current Characteristics of Superconductor Weak-Link Junctions,” *J. Appl. Phys.*, vol. 39, no. 7, pp. 3113–3118, Jun. 1968, doi: 10.1063/1.1656743.

[16] J. Taylor and C. J. Fourie, “lOverview of Superconducting Digital Electronics,” no. October, 2009.

[17] T. A. Fulton and L. N. Dunkleberger, “Lifetime of the zero-voltage state in Josephson tunnel junctions,” *Phys. Rev. B*, vol. 9, no. 11, pp. 4760–4768, Jun. 1974, doi: 10.1103/PhysRevB.9.4760.

[18] J. M. Rowell, “Magnetic Field Dependence of the Josephson Tunnel Current,” *Phys. Rev. Lett.*, vol. 11, no. 5, pp. 200–202, Sep. 1963, doi: 10.1103/PhysRevLett.11.200.

[19] M. J. Cyster, J. S. Smith, N. Vogt, G. Opletal, S. P. Russo, and J. H. Cole, “Simulating the fabrication of aluminium oxide tunnel junctions,” *npj Quantum Inf.*, vol. 7, no. 1, pp. 20–22, 2021, doi: 10.1038/s41534-020-00360-4.

[20] L. J. Zeng *et al.*, “Direct observation of the thickness distribution of ultra thin AlOx barriers in Al/AlOx/Al Josephson junctions,” *J. Phys. D. Appl. Phys.*, vol. 48, no. 39, 2015, doi: 10.1088/0022-3727/48/39/395308.

[21] R. Firouzmandi, “Fabrication and characterization of Al/AlOx/Al Josephson

junctions for superconducting qubits," *PhD thesis*, 2021.

[22] G. J. Dolan, "Offset masks for lift-off photoprocessing," *Appl. Phys. Lett.*, vol. 31, no. 5, pp. 337–339, Sep. 1977, doi: 10.1063/1.89690.